Advanced human iPSC-based modelling of *LMNA*-related congenital muscular dystrophy enables development of targeted genetic therapies for muscle laminopathies

Daniel P. Moore[1,2], Heather B. Steele-Stallard[1], Luca Pinton[1,2,3], Valentina Maria Lionello[1,2], Lucia Rossi[1,2], Artadokht Aghaeipour[1,2], Salma Jalal[1,2], Cherry Tsz Yan Wong[1,2], Angela Clara-Hwang[1,2], Gisèle Bonne[4], Peter S. Zammit[3,±], Francesco Saverio Tedesco[1,2,5,±,*]

[1]Department of Cell & Developmental Biology, Division of Biosciences, University College London, London WC1E 6DE, UK

[2]The Francis Crick Institute, London NW1 1AT, UK

[3]Randall Centre for Cell & Molecular Biophysics, King's College London, SE1 1UL, London, UK

[4]Sorbonne Université, INSERM, Institut de Myologie, Centre de recherche en Myologie, Paris, France

[5]Dubowitz Neuromuscular Centre, Great Ormond Street Hospital and UCL Great Ormond Street Institute of Child Health, London, UK.

[±]Senior authors

*Correspondence: f.s.tedesco@ucl.ac.uk

HIGHLIGHTS

- *LMNA*-mutant iPSCs undergo efficient skeletal myogenesis upon transgene-free, small molecule-based lineage-directed differentiation.
- *LMNA*-mutant iPSCs recapitulate hallmark disease-associated nuclear phenotypes and show a pro-inflammatory transcriptional profile
- *LMNA*-mutant iPSC-derived muscle cells enable testing of genetic therapies
- CRISPR-edited L-CMD iPSC-derived myogenic cells show amelioration of disease-associated phenotypic readouts

ABSTRACT

LMNA-related congenital muscular dystrophy (L-CMD) is amongst the most severe forms of laminopathies, which are diseases caused by pathogenic variants in the *LMNA* gene. *LMNA* encodes the proteins LAMINs A and C, which assemble with LAMIN B1 and B2 to form the nuclear lamina: a meshwork providing structural stability to the nucleus that also regulates chromatin organisation and gene expression. Research into L-CMD mechanisms and therapies i hindered by lack of humanised, tissue-specific models that accurately recapitulate disease phenotypes. We previously reported that *LMNA*-mutant induced pluripotent stem cell (iPSC)-derived skeletal muscle cells have nuclear shape abnormalities and LAMIN A/C protein mislocalisation. Here, we expand the selection of L-CMD patient-derived iPSCs and validate disease-associated readouts using a transgene-free based protocol which more accurately mimics skeletal myogenesis. Results showed no defects in developmental myogenesis, but recapitulation of pathological nuclear shape abnormalities in 2D and 3D cultures, nuclear envelope protein mislocalisation and transcriptomic alterations across multiple pathogenic *LMNA* variants. We then utilised this platform to assess *LMNA* gene editing strategies. CRISPR-based exon removal generated stable RNA and protein LAMIN A/C species, without significant normalisation of nuclear morphological phenotypes. Conversely, precise editing of the same mutation showed complete reversal of disease-associated nuclear morphometrics. Our data provide the foundation for a humanised *in vitro* disease and therapy modelling platform for this complex and severe muscle disorder.

GRAPHICAL ABSTRACT (created with BioRender.com)

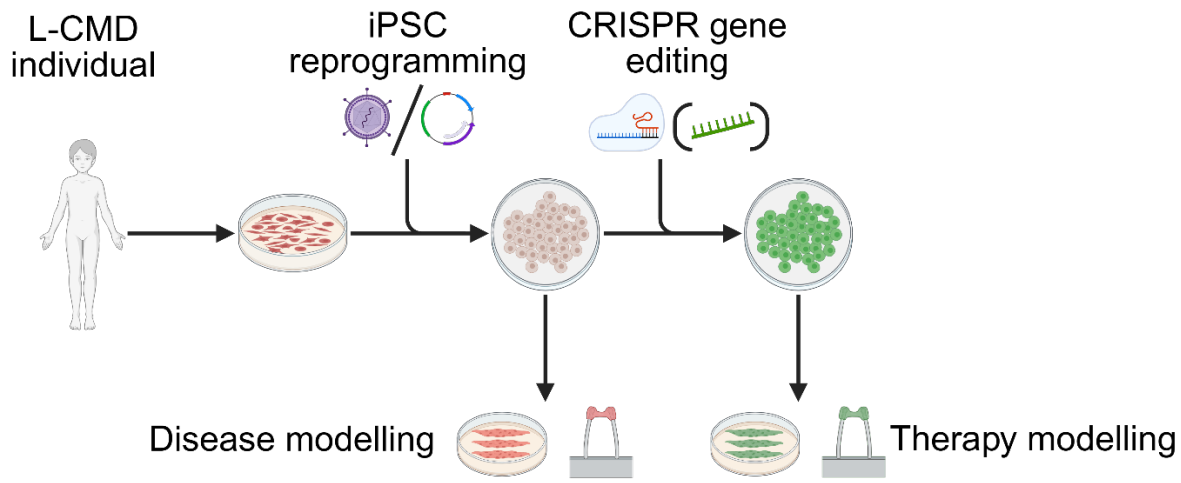

KEYWORDS

iPSCs; LMNA; laminopathies; disease modelling; 3D cultures; gene editing.

INTRODUCTION

Laminopathies are a group of genetic diseases caused primarily by mutations in the *LMNA* gene. *LMNA* encodes LAMIN A/C, which assemble with LAMIN B1 and B2 to form the nuclear lamina: a meshwork providing structural stability to the nucleus[1]. At least 16 diseases are caused by mutations in the *LMNA* gene, amongst which the most common and severe are those affecting striated muscle tissues. In particular, *LMNA*-related congenital muscular dystrophy (L-CMD) is a severe paediatric form of cardiac and skeletal striated muscle laminopathy, clinically characterised by early onset muscle weakness and wasting and dropped head syndrome. Sudden death in the first decade of life is common due to cardio-respiratory failure[2,3]. The precise pathological mechanisms of laminopathies remain elusive and likely varies by mutation and individual.

Two non-mutually exclusive hypotheses have emerged as primary candidate mechanisms for pathogenesis. The mechanical stress hypothesis focuses on the breakdown of the mechanoresponsive properties of the nuclear lamina when mutated. A key phenotype of laminopathies is presence of abnormally shaped nuclei, which has been modelled in *in vitro* and *in vivo* studies[4–11]. Impaired mechanoresponse can lead to mispositioning of nuclei within muscle tissues, potentially perturbing myonuclear domain positioning[7,12]. Furthermore, many *LMNA*-mutations increase susceptibility of nuclei to rupture, the functional consequences of which can include loss of genetic and nucleoplasmic material, activation of inflammatory response pathways and cell death[13–16]. Ultimately, these mechanisms may be particularly relevant in mechanically active tissues such as striated muscle, which is the most affected tissue in laminopathies.

The gene regulation hypothesis states that pathological changes in transcription occur due to altered chromatin organisation and contact with mutant LAMIN A/C. Studies across various model systems and laminopathy subtypes have revealed alterations to LAMIN A/C-chromatin interactions at lamina-associated domains, gene enhancers, and transcription start sites, as well as altered interactions with the epigenetic repressive polycomb group proteins[17–22]. Two studies have examined transcriptional dysregulation caused by *LMNA* mutations in skeletal muscle cells. The first, revealed alterations to signalling pathways such as MAPK, Akt/mTOR, AMPK and proteostasis, via RNA-sequencing of biopsied muscle tissue from a patient carrying the LAMIN A/C p.G449V mutation[23]. More recently, a study identified disruption of metabolism, ECM and fibrosis, de-repression of alternative fate genes and disrupted splicing pathways as integrative mechanisms of pathogenesis in primary myoblast lines from patients with Emery-Dreifuss muscular dystrophy (EDMD),

caused by mutations in *LMNA*, *TMEM214*, *PLPP7*, *SUN1*, *SYNE1*, *EMD* and *FHL1*[24]. However, the impact of variants causative of L-CMD (the most severe striated muscle laminopathy) on the transcriptome remains unexplored, possibly due to the invasive sampling required in such a severe, early onset condition.

While these studies highlight general pathways and mechanisms of laminopathy pathogenesis, the lack of effective, humanised models of L-CMD prevent examination of tissue and disease-specific pathomechanisms. A concern when using non-human models of laminopathies, is the inability of these models to recapitulate the precise pathogenetic events leading to disease. For example, murine models typically require homozygous *LMNA* mutations to elicit a phenotype, while the majority of human mutations are heterozygous, with a dominant negative disease mechanism[25]. Therefore, humanised model systems using primary, immortalised or iPSC-derived myogenic cells are being used to investigate tissue and disease specific pathomechanisms of laminopathies. Despite this, research into L-CMD using humanised model systems remains limited. Primary and immortalised human myoblasts have been used to study mechanotransduction defects and nuclear shape changes in miniaturised engineered muscle models[4,26–29]. However, given that L-CMD is a rare disease and no longer requires invasive biopsy for diagnosis, these cell lines are limited in number and difficult to access for the wider research community. To overcome this limitation, we have harnessed the controllable proliferative and differentiative capacity of iPSCs to study laminopathies in a humanised, tissue specific-manner in monolayer and 3D engineered muscle tissues, enabling modelling of nuclear shape abnormalities and providing initial evidence of iPSC potential in laminopathy research[9,30]. Nonetheless, the full potential of *LMNA*-mutant iPSC to answer key questions in laminopathies such genotype-phenotype correlations, impact

on human skeletal myogenesis, transcriptional alterations and capacity to predict efficacy of novel therapeutic strategies, remains unexploited.

Here, we expand the iPSC-based modelling platform to include a novel L-CMD line and examine the impact of different *LMNA* mutations on myogenesis, model nuclear morphological abnormalities and protein mislocalisation phenotypes and analyse transcriptomic alterations in *LMNA*-mutant iPSC skeletal myogenic derivatives in 2D and 3D culture systems. Furthermore, we use this iPSC-based platform to examine multiple CRISPR-Cas9 based therapeutic approaches for the amelioration of disease-associated phenotypes in L-CMD.

RESULTS

Human iPSCs harbouring pathogenic *LMNA* variants undergo efficient skeletal myogenesis upon transgene-free, small molecule-based differentiation

We previously reported that cellular features of skeletal muscle laminopathies can be modelled using human iPSCs carrying pathogenic *LMNA* variants differentiated into skeletal myogenic cells by overexpressing the myogenic regulator MYOD[9]. However, other studies have demonstrated impaired skeletal myogenic differentiation in *LMNA*-mutant or null cells[5,31–33]. Therefore, to determine whether pathogenic *LMNA* variants interfere with human developmental skeletal myogenesis *in vitro*, we selected two readily available, fully characterised *LMNA*-mutant iPSCs (*LMNA*^{K32del}, hPSCreg: CMDi003-A; *LMNA*^{R249W}, hPSCreg: CMDi004-A) alongside our novel *LMNA*^{L302P} iPSC line (characterisation in Figure S1) into skeletal myogenic progenitors and then terminally differentiated myotubes using a transgene-free, small molecule-based protocol, modelling developmental myogenesis[34]. These 3 iPSC lines were associated with the severe L-CMD phenotype and included different types of pathogenic

mechanisms (e.g. missense and deletion), frequency (relatively common such as *LMNA*^{R249W} vs. ultra rare such as *LMNA*^{L302P}) regions of the gene/protein affected (exons 1, 4 and 5 respectively). Two healthy donor iPSC lines were used as controls.

We first confirmed presence of the pathogenic *LMNA* variants (K32del, R249W and L302P; Figure 1A) as well as presence of pluripotency-associated factors through immunostaining for SOX2, NANOG and OCT4 (Figure 1B, C). LAMIN A/C is known to be absent in pluripotent cells and progressively expressed in most somatic tissues as differentiation proceeds[35], and indeed undifferentiated iPSC colonies were negative as expected (Figure 1B).

To model developmental myogenesis, we used a transgene-free, small molecule-based protocol to differentiate these 3 iPSC lines into skeletal myogenic progenitors and then terminally differentiated myotubes[34]. To confirm commitment to the myogenic lineage we immunostained for the master transcriptional regulator of muscle differentiation MYOD. MYOD and LAMIN A/C were detected in all cell lines, indicating successful myogenic commitment (Figure 1D). We then induced terminal skeletal myogenic differentiation by allowing cells to reach confluency, followed by serum starvation. Cells fused over the course of 2-4 days to form multinucleated, myosin-positive myotubes with LAMIN A/C-positive myonuclei (Figure 1D). Interestingly, we observed that non-differentiated cells often expressed visibly less LAMIN A/C as indicated by decreased fluorescent signal compared to myonuclei. To examine whether a differentiation defect was present in the *LMNA*-mutant lines, we analysed the differentiation index. Results showed no significant myogenic differentiation defect in any of the *LMNA* mutant lines versus controls (Figure 1E; Controls 1 and 2 80.07 ± 0.60 % and 80.68 ± 12.69 % respectively, K32del, R249W and L302P 80.27 ± 4.53 %, 70.35 ± 5.36 % and 82.32 ± 3.09 % respectively). These

data show that dominant-negative *LMNA* variants do not impair exit from pluripotency and differentiation of human iPSCs into the skeletal muscle lineage *in vitro*.

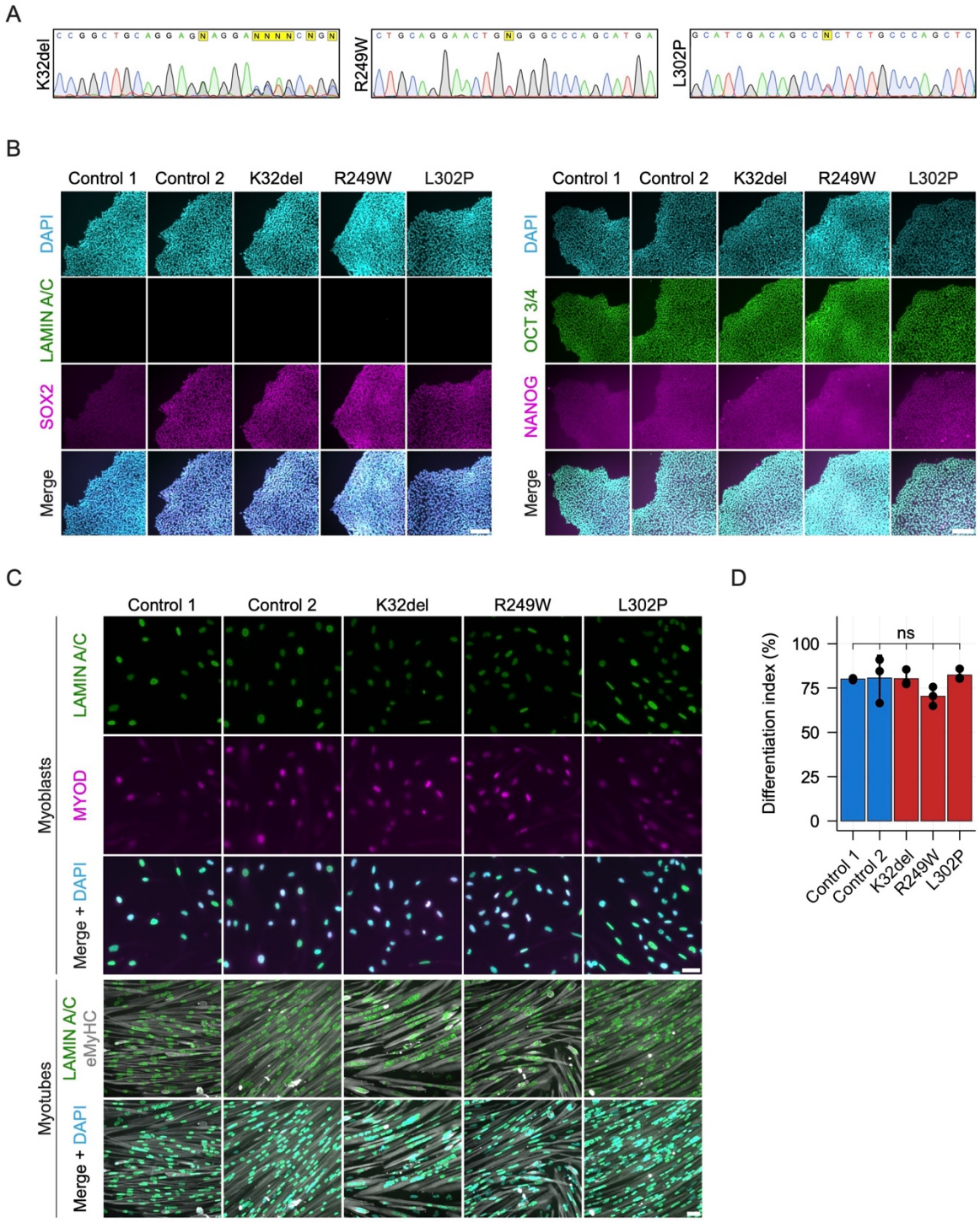

Figure 1. L-CMD iPSCs undergo efficient transgene-free, small molecule-based skeletal myogenesis *in vitro*.

(A) Sanger sequencing electropherograms confirming presence of heterozygous *LMNA* pathogenic variants in the cell lines used.

(B) Immunostaining of NANOG and OCT3/4, SOX2 and LAMIN A/C in iPSCs. Nuclei counterstained with DAPI. Scale bar 100µm.

(C) Immunostaining of LAMIN A/C and MYOD in control and LMNA-mutant myoblasts and of LAMIN A/C and embryonic myosin heavy chain (eMyHC) in control and LMNA-mutant myotubes. Counterstained with DAPI. Scale bar 50 µm.

(D) Differentiation index of control and LMNA-mutant myotubes. One-way ANOVA with Tukey's post-hoc tests for comparisons to controls. Three independent passages were analysed per cell line (N = 3). 1311 – 3562 nuclei were analysed per cell line, per repeat. ns $p>0.05$. Dots show mean value of each replicate. Whiskers show standard deviation.

LMNA-mutant, iPSC-derived skeletal myotubes have abnormal nuclear morphology, nuclear envelope protein localisation and nucleoplasmic reticulum

Having efficiently generated *LMNA*-mutant skeletal myotubes from multiple L-CMD iPSCs, we then assessed presence of hallmark laminopathy nuclear shape abnormalities[9]. We observed a range of myonuclear dysmorphism in *LMNA*-mutant populations that we broadly categorised as "Normal", "Deformed", "Blebbed", "Elongated" or "String" (Figure 2A). To examine whether these categories were present in significantly larger numbers in *LMNA*-mutant cell lines versus controls, we quantified the proportion of each of these categories in a blinded manner (Figure 2B). Each *LMNA*-mutant line had significantly reduced proportions of "Normal" myonuclei versus controls (K32del: 55.09 ± 3.88 %; R249W: 48.65 ± 4.45 %; L302P: 68.15 ± 2.17 %). Overall, "Deformed" was the most common dysmorphic classification in *LMNA*-mutant myonuclei (K32del: 20.84 ± 3.34 %; R249W: 25.19 ± 1.44 %; L302P: 20.44 ± 1.19 %). Blebbed was the next most frequent classification in K32del (K32del: 18.47 ± 9.00 %; R249W: 9.42 ± 1.09 %; L302P: 4.93 ± 0.85 %), while elongated myonuclei were the second most common dysmorphism in R249W and L302P (K32del: 11.68 ± 31.89 %; R249W: 21.07 ± 5.23 %; L302P: 6.39 ± 3.67 %). String myonuclei were the most severe and least common dysmorphism in all *LMNA*-mutant

lines and the only one not observed in both Controls (K32del: 1.54 ± 2.51 %; R249W: 3.63 ± 1.05%; L302P: 1.22 ± 0.52%).

To complement this analysis, we quantified additional nuclear morphometric parameters. We assessed nuclear circularity ratio (NCR)[9] and *LMNA*-mutant cell lines had significantly fewer circular nuclei than healthy controls (Figure 2C; control myonuclei: 0.779 ± 0.016; control non-myonuclei: 0.805 ± 0.042; *LMNA*-mutant myonuclei: 0.73 ± 0.053; *LMNA*-mutant non-myonuclei: 0.67 ± 0.047). In *LMNA*-mutant cell lines, a population of severely dysmorphic myonuclei and non-myonuclei were observed, corresponding to NCR scores of <0.5, which were typically not present in control cells. Nuclear perimeter and nuclear area as were also measured revealing significantly increased myonuclear and non-myonuclear perimeter in *LMNA*-mutant lines (Figure S2A; control myonuclei: 47.93 ± 2.67 μm; control non-myonuclei: 24.19 ± 2.14 μm; *LMNA*-mutant myonuclei: 53.77 ± 3.24 μm; *LMNA*-mutant non-myonuclei: 71.69 ± 5.45 μm). We did not observe an increase in nuclear area in either myonuclei or non-myonuclei between *LMNA*-mutants and controls (control myonuclei: 143.13 ± 17.01 μm; control non-myonuclei: 233.21 ± 25.83 μm^2; *LMNA*-mutant myonuclei: 159.06 ± 14.97 μm^2; *LMNA*-mutant non-myonuclei: 270.89 ± 28.96 μm^2; Figure S2B).

Cellular phenotypes of laminopathies also include mislocalisation of nuclear lamins, with striated muscle laminopathy-causing mutations having a particular propensity to form LAMIN protein aggregates[36]. Investigating LAMIN A/C and LAMIN B1 mislocalisation showed each *LMNA*-mutant cell line exhibited mislocalisation of both LAMIN A/C and B1 which were typically characterised by aggregations of protein or localised depleted immunosignal (Figure 2D). The proportion of myonuclei showing LAMIN A/C mislocalisation in K32del, R249W and L302P were 45.51 ± 8.98 %, 30.10 ± 1.09 % and 23.44 ± 5.61 % respectively (Figure 2E). LAMIN B1 mislocalisation

occurred in 18.80 ± 5.89 % of K32del myonuclei, 18.85 ± 4.51 % of R249W myonuclei and 20.70 ± 5.41 % of L302P myonuclei (Figure 2F).

We then examined the nucleoplasmic reticulum in myonuclei of the same cultures. These are invaginations of the nuclear envelope which have been proposed to play roles in calcium signalling, structural support and transport of small molecules across the nuclear envelope. These structures are lined by the nuclear lamina and as such, we hypothesized that a destabilisation of nuclear lamin proteins may lead to the formation of less nucleoplasmic reticulum. Like LAMIN A/C and B1 mislocalisation, we quantified the number of myonuclei displaying nucleoplasmic reticula across *LMNA*-mutant lines and healthy controls (Figure 2G). We observed significantly reduced numbers of myonuclei with nucleoplasmic reticula in all *LMNA*-mutant lines assessed versus both controls (62.46 ± 6.52 % and 51.07 ± 3.44 % in Control 1 and 2 respectively; 27.47 ± 7.47 %, 19.55 ± 5.73 % and 23.57 ± 10.04 % in K32del, R249W and L302P, respectively; Figure 2H).

We previously showed that modelling laminopathies in 3D engineered muscle tissues exacerbates myonuclear dysmorphic phenotypes in *LMNA*-mutant cells[9]. We therefore generated engineered muscle tissues using transgene-free iPSC-derived myoblasts to study nuclear morphologies (Figure 2H; Figure S2C). Comparisons of *LMNA*-mutant myonuclei versus control lines revealed a clear myonuclear elongation phenotype in all *LMNA*-mutant 3D engineered muscles compared to healthy controls (Figure 2I). Together, these results validate myonuclear shape and protein mislocalisation as robust phenotypes across iPSC myogenic differentiation protocols, supporting the use of *LMNA*-mutant iPSC derivatives in disease modelling for laminopathies.

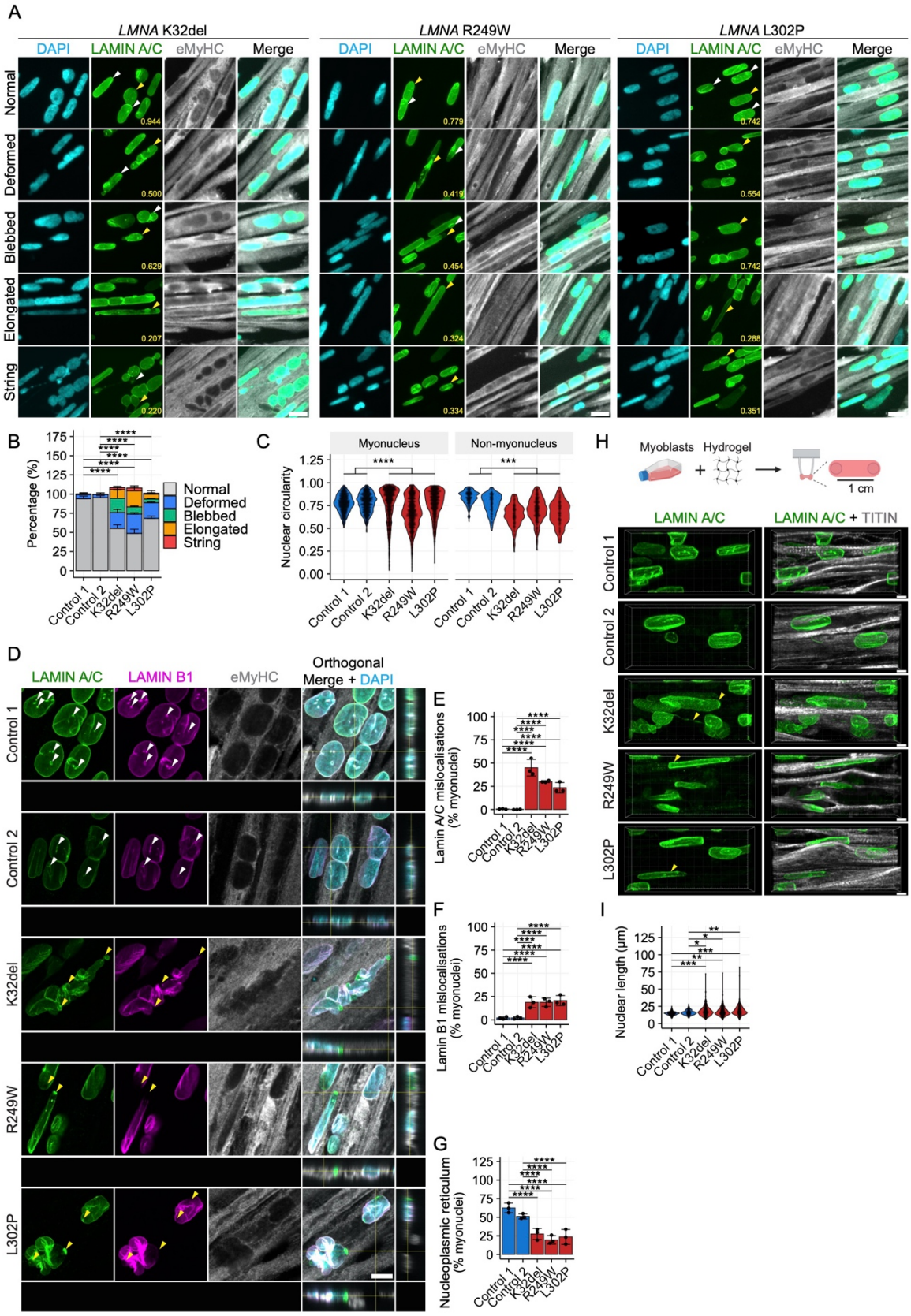

Figure 2. L-CMD iPSC-derived myonuclei show pathological laminopathy phenotypes in monolayer culture and 3D engineered muscles.

(A) Immunostaining of LAMIN A/C and embryonic myosin heavy chain (eMyHC) showing representative images of five nuclear morphology classifications are displayed: Normal, Deformed, Blebbed, Elongated, and String.

(B) Proportion of nuclear shape classifications in myotube nuclei. Nuclei with more than one type of abnormality (e.g. elongated and deformed) were scored twice meaning totals can exceed 100%. Nuclei were considered elongated if they had a major axis length >30 µm. Number of normal shaped nuclei were compared between *LMNA*-mutants and controls for fractional logistic regression with Tukey's correction for pairwise comparisons. Three independent passages were analysed per cell line (N=3). 96-291 myotube nuclei were analysed per cell line, per repeat. *** $p<0.001$; **** $p<0.0001$. Data presented as stacked bar chart. Whiskers show standard deviation.

I Graphs showing quantification of nuclear circularity. Beta regression with Bonferroni correction for pairwise comparisons. Data presented as scatter plots showing measurements of all nuclei across repeats with violin plots showing distribution of measurements. Three independent passages were analysed per cell line (N=3). 205-622 myotube nuclei and 50-174 non-myotube nuclei were analysed per cell line, per repeat. *** $p<0.001$; **** $p<0.0001$.

(D) Representative immunostain of LAMIN A/C, LAMIN B1 and eMyHC. Counterstained with DAPI. Z-stack images of control and LMNA-mutant nuclei are displayed as a single Z-slice, with orthogonal view. White arrowheads indicate nucleoplasmic reticulum, yellow arrows indicate LAMIN mislocalisation. Scale bar 20 µm.

(E, F) (E) LAMIN A/C mislocalisation (F) LAMIN B1 mislocalisation. Fractional logistic regression with Tukey's post hoc test for pairwise comparisons. Three independent passages were analysed per cell line (N = 3). A total of 119 – 347 nuclei were analysed per cell line, per repeat. **** $p<0.0001$. Dots represent the mean value of one replicate. Whiskers indicate the standard deviation.

(G) Quantification of nucleoplasmic reticulum positive nuclei in control and LMNA-mutant myotube nuclei. Fractional logistic regression with Tukey's post hoc test for pairwise comparisons. Three independent passages were analysed per cell line (N = 3). 107 – 246 nuclei were analysed per cell line, per repeat. * $p<0.05$; ** $p<0.01$; *** $p<0.001$. Dots show mean value of one replicate. Whiskers indicate standard deviation.

(H) Schematic diagram showing generation of 3D engineered muscles and immunostain for LAMIN A/C and Titin in 3D engineered muscles. Scale bar 5 µm.

(I) Graphs showing quantification of myonuclear length in 3D engineered muscles. One-way ANOVA with Tukey's correction for pairwise comparisons. Data presented as scatter plots showing measurements of all nuclei across repeats with violin plots showing distribution of measurements. Three independent passages were analysed per cell line (N=3). 4 - 188 nuclei were analysed per cell line, per repeat. * $p<0.05$; ** $p<0.01$; *** $p<0.001$; **** $p<0.0001$.

Transcriptomic analysis of *LMNA*-mutant skeletal myogenic iPSC derivatives reveals a pro-inflammatory profile

Having modelled morphological nuclear phenotypes in *LMNA*-mutant muscle cells, we next sought to examine whether severely dysmorphic laminopathic myonuclei remain transcriptionally active and whether the transcriptional profile of the cells was altered

compared to control cell lines. To do this, we first assessed the transcriptional status of *LMNA*-mutant myonuclei by labelling nascent RNA with the nucleoside analogue 5-ethynyl uridine (Figure 3A). Co-immunostaining with eMyHC and LAMIN A/C confirmed that all *LMNA*-mutant (including severely dysmorphic) myonuclei remain transcriptionally active (Figure 3B).

To examine transcriptional changes in *LMNA*-mutant iPSC derivatives, we performed bulk RNA sequencing of control and mutant myoblasts and myotubes. Following batch correction, we observed that control and *LMNA*-mutant samples clustered separately following principal component analysis in both myoblast and myotube samples, though differences between control cell lines were present due to their different genetic background (Figure 3C, D).

Differential gene expression analysis revealed 1070 upregulated genes and 974 downregulated genes in *LMNA*-mutant myoblasts compared to controls (Figure 3E). For *LMNA*-mutant myotubes, we found 844 upregulated genes and 628 downregulated genes compared to controls (Figure 3F).

As two non-isogenic controls were used to examine transcriptional changes and these cell lines were transcriptionally distinct from each other in addition to being distinct from *LMNA*-mutants, we used gene set enrichment analysis (GSEA) to examine differential hallmark gene sets between *LMNA*-mutant and control cell lines. Notably, comparison of *LMNA*-mutant myoblasts to control lines revealed enrichment for hallmark gene sets related to inflammatory signalling including “Inflammatory response”, “TNFA signalling via NFκβ”, “Interferon alpha response” and “Interferon gamma response”. Such enriched gene sets indicate that cell autonomous inflammatory signalling may be altered in *LMNA*-mutant muscle cells potentially leading to activation of stress response pathways. Interestingly, “Myogenesis” was

negatively enriched in *LMNA*-mutant myoblasts, despite our earlier observations that *LMNA*-mutant myogenic cells differentiate as well as controls (Figure 3G).

There were broadly similar transcriptional changes in *LMNA*-mutant myotubes when comparing to controls, including enrichment of the same inflammatory pathways “TNFA signalling via NFκβ” and “Inflammatory response”. Additionally, “P53 pathway” emerged as an enriched pathway in *LMNA*-mutant myotubes, indicating that these cells may be more transcriptionally primed for apoptotic cell death than controls (Figure 3H). Together these results indicate that *LMNA*-mutant muscle cells have a cell-autonomous inflammatory transcriptional profile which may contribute to the severity of L-CMD pathophysiology.

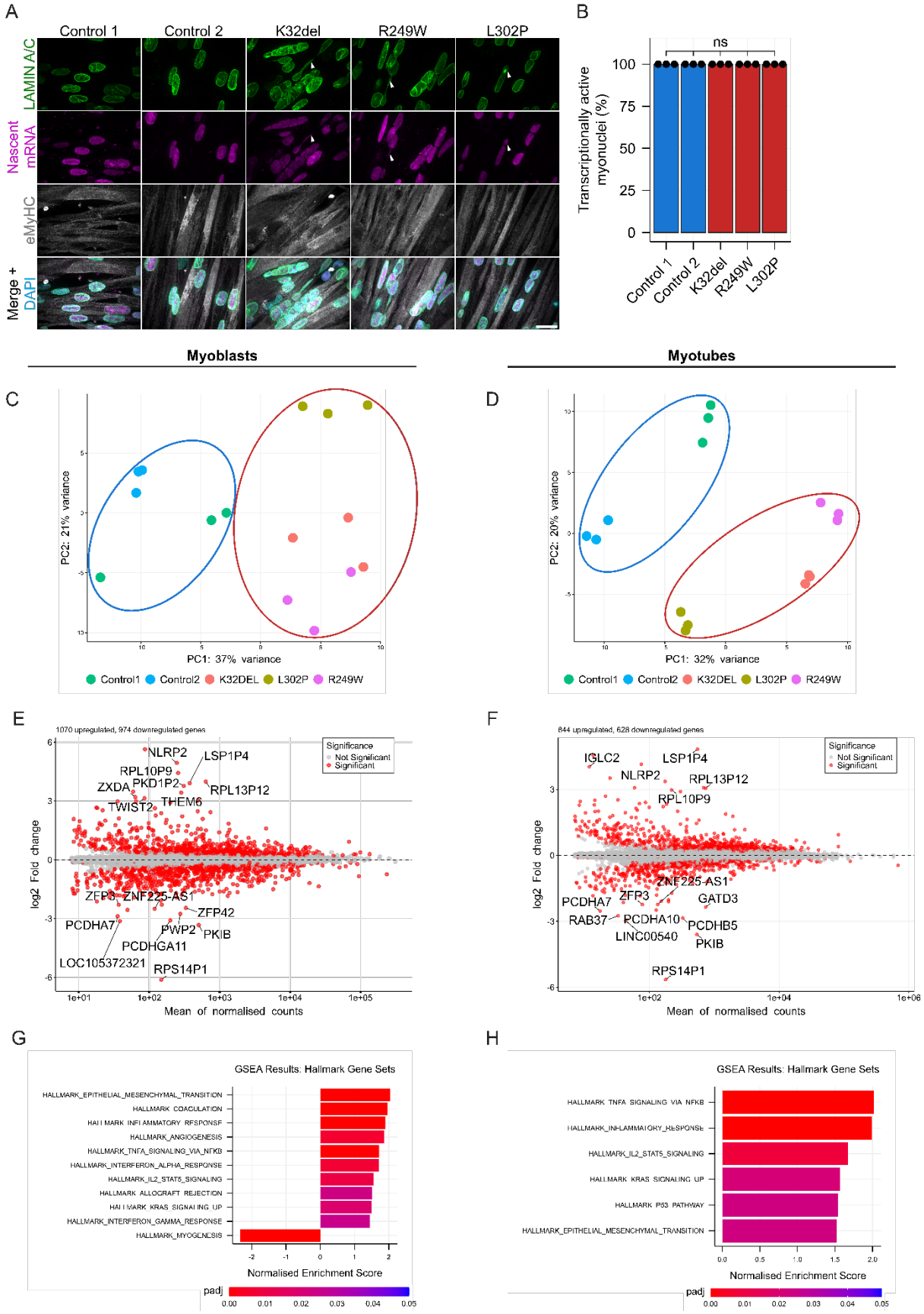
A
Control 1
Control 2
K32del
R249W
L302P
LAMIN A/C
Nascent mRNA
eMyHC
Merge + DAPI
B
ns
Transcriptionally active myonuclei (%)
100
75
50
25
0
Control 1
Control 2
K32del
R249W
L302P
Myoblasts
Myotubes
C
PC2: 21% variance
PC1: 37% variance
Control1 Control2 K32DEL L302P R249W
D
PC2: 20% variance
PC1: 32% variance
Control1 Control2 K32DEL L302P R249W
E
1070 upregulated, 974 downregulated genes
Significance
Not Significant
Significant
NLRP2
LSP1P4
RPL10P9
ZXDA
PKD1P2
RPL13P12
TWIST2
THEM6
ZFP3
ZNF225-AS1
ZFP42
PCDHA7
PWP2
PKIB
PCDHGA11
LOC105372321
RPS14P1
log2 Fold change
Mean of normalised counts
F
844 upregulated, 628 downregulated genes
Significance
Not Significant
Significant
IGLC2
LSP1P4
NLRP2
RPL13P12
RPL10P9
ZNF225-AS1
PCDHA7
ZFP3
GATD3
RAB37
PCDHA10
PCDHB5
LINC00540
PKIB
RPS14P1
log2 Fold change
Mean of normalised counts
G
GSEA Results: Hallmark Gene Sets
HALLMARK_EPITHELIAL_MESENCHYMAL_TRANSITION
HALLMARK_COAGULATION
HALLMARK_INFLAMMATORY_RESPONSE
HALLMARK_ANGIOGENESIS
HALLMARK_TNFA_SIGNALING_VIA_NFKB
HALLMARK_INTERFERON_ALPHA_RESPONSE
HALLMARK_IL2_STAT5_SIGNALING
HALLMARK_ALLOGRAFT_REJECTION
HALLMARK_KRAS_SIGNALING_UP
HALLMARK_INTERFERON_GAMMA_RESPONSE
HALLMARK_MYOGENESIS
Normalised Enrichment Score
padj
H
GSEA Results: Hallmark Gene Sets
HALLMARK_TNFA_SIGNALING_VIA_NFKB
HALLMARK_INFLAMMATORY_RESPONSE
HALLMARK_IL2_STAT5_SIGNALING
HALLMARK_KRAS_SIGNALING_UP
HALLMARK_P53_PATHWAY
HALLMARK_EPITHELIAL_MESENCHYMAL_TRANSITION
Normalised Enrichment Score
padj

Figure 3. Transcriptomic profile of L-CMD iPSC-derived skeletal myogenic cells.

(A) Labelling of nascent RNA with alkyne-modified 5-ethynyl uridine and fluorescently tagged azide, co-immunostain of LAMIN A/C and embryonic myosin heavy chain (eMyHC). Nuclei counterstained with DAPI. Scale bar 20µm.

(B) Quantification of transcriptionally active myonuclei. Fractional logistic regression with post-hoc pairwise comparisons using *Tukey's* method. Three independent passages were analysed per cell line (N = 3). A total of 39-71 nuclei were analysed per cell line per repeat. ns $p \geq 0.05$. Dots represent the mean of one replicate.

(C, D) PCA plots of control and *LMNA*-mutant (C) myoblasts and (D) myotubes. Blue circle indicates control cell lines and red circle indicates *LMNA*-mutant cell lines.

(E, F) MA plots of *LMNA*-mutant versus control (E) myoblasts and (F) myotubes. Significantly differentially expressed genes are indicated in red while non-significant genes are indicated in grey.

(G, H) Gene set enrichment analysis (GSEA) of *LMNA*-mutant versus control (G) myoblasts and (H) myotubes. Hallmark gene sets were used and significantly enriched gene sets are displayed as a bar chart ordered by normalised enrichment score (NES).

From disease to therapy modelling: L-CMD iPSC-derived myogenic cells to assess genetic therapies

Having established that the iPSC-based platform could model morphological and transcriptomic readouts in laminopathy skeletal myotubes, we sought to examine whether we could use our model system as a tool to development and test gene therapy strategies. Our previous work has shown that *LMNA* exon 5 (and, to a lesser extent, exon 3) is potentially amenable to exon skipping, as removal of heptad repeats should not disrupt assembly of a-helical coils, making it applicable to multiple patients sharing pathogenic variants within the same exon[8]. Therefore, targeting a mutation in exon 5 would enable us to examine multiple modalities of gene therapy within our model system. To date, 243 individuals with mutations in *LMNA* exon 5 have been reported, with 52 % of affected individuals having a striated muscle laminopathy phenotype (Figure 4A, B; www.umd.be/LMNA/, and G Bonne, R Ben Yaou, personal communication). We first used AlphaFold 2 to model predicted wild-type, L302P and exon 5-removed (Δexon 5) LAMIN A and C protein dimers to predict the impact of

exon removal on protein structure and dimerization. Homodimers of Δexon 5 LAMIN proteins were predicted to assemble in a coiled-coil confirmation typical of LAMIN dimers, whereas Δexon 5 and wild-type/L302P heterodimers were predicted to disrupt to dimerization due to mismatched protein length (Figure S3A). We then investigated whether internally truncated lamins could be expressed, produced and assembled in human cells. HeLa cells were transduced with retroviral vectors overexpressing WT LAMIN A, LAMIN A Δexon 3 or LAMIN A Δexon 5, all linked to a green fluorescent protein by an IRES site. Analysis of overexpressing cells showed correct production of the Δexon 5, but not the Δexon 3 internally truncated LAMIN A protein (Figure 4C, D), supporting further development of a genetic therapy strategy to skip or excise exon 5, alongside an alternative approach based upon precise correction of the L302P, both CRISPR-based.

We targeted introns on both sides of exon 5 to excise it from the gDNA, thereby removing the mutation-containing exon entirely (Δexon 5) and in parallel, we corrected the *LMNA* L302P mutation in iPSCs using homology directed repair to generate edited wild-type (e-WT) iPSCs (Figure 4E; Figure S3B, C). We then differentiated these cells into myogenic precursors and examined formation of the expected RNA and protein products. e-WT cells produced cDNA and protein products of the same size as the L302P cells, while Δexon 5 cells showed shortened stable cDNA and protein species, corresponding to the shortened LAMIN species produced (Figure 4F; Figure S3D, E). While generating clones of Δexon 5 lines, we also identified clones which had the expected gDNA band size, but abnormal cDNA and protein products which likely resulted from unwanted DNA recombination events (Figure S3F, G). Sanger sequencing of cDNA confirmed the expected genetic modifications (Figure 4G).

To examine whether CRISPR-based gene editing of the *LMNA* gene may impact differentiation capacity of the cells, we quantified differentiation index of the e-WT, L302P and Δexon 5 lines. Each of the cell lines produced multinucleated, myosin-positive myotubes as expected (Figure 4H), with similar differentiation index (Figure 4I; L302P 78.82 ± 9.56 %, Δexon 5 82.23 ± 10.29 % and e-WT 76.66 ± 9.85 %).

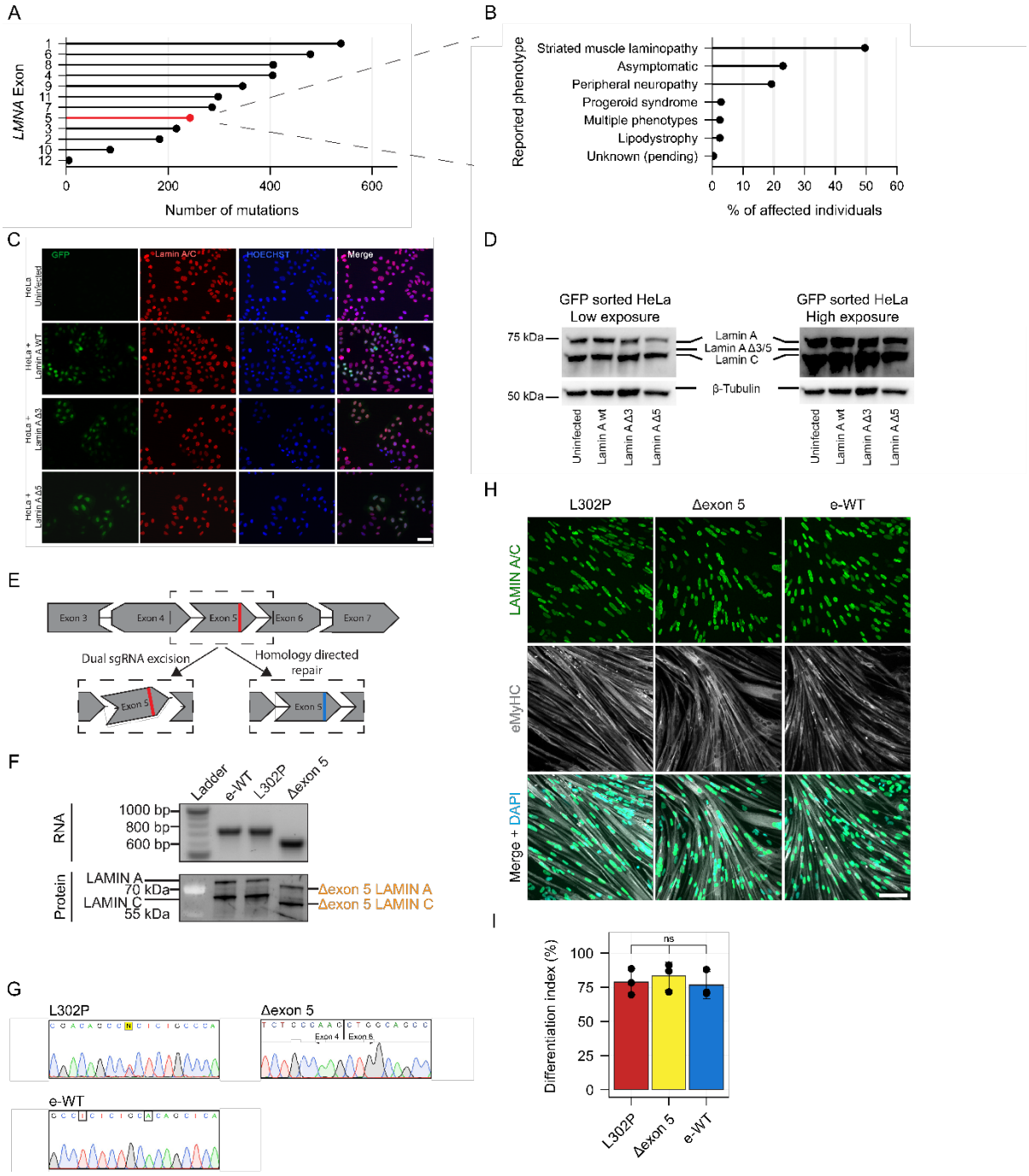

Figure 4. Two alternative CRISPR-based gene editing strategies targeting the *LMNA*^{L302P} variant in iPSCs.

(A) Graph showing the number of pathogenic variants reported in each *LMNA* exons in the UMD database.

(B) Graph showing the proportion of clinical phenotypes associated with pathogenic variants in *LMNA* exon 5.

(C) Immunostaining of HeLa cells transduced with LAMIN A WT, Δexon 3 (as an additional control), or Δexon 5 constructs. GFP expressed through an IRES. Scale bar 100 µm.

(D) Western blot of FACS sorted HeLa cells for LAMIN A/C, showing the truncated Δexon 5 band at high exposure.

(E) Schematic diagram of CRISPR editing strategies used, targeting the *LMNA*^{L302P} variant.

(F) Sanger sequencing chromatograms of *LMNA*^{L302P} and CRISPR edited cells.

(G) PCR of *LMNA* exon 5 region cDNA and western blot for LAMIN A/C in *LMNA*^{L302P} and CRISPR edited cell lines.

(H) Immunostaining of LAMIN A/C and eMyHC. Nuclei counterstained with DAPI. Scale bar 100 µm.

(I) Quantification of differentiation index. One-way ANOVA with Tukey's post hoc comparisons to controls. Three independent passages were analysed per cell line (N = 3). 236-408 nuclei were analysed per cell line, per repeat. ns $p \geq 0.05$. Dots represent mean value of one replicate. Whiskers show standard deviation.

L-CMD iPSC-derived skeletal myogenic cells enable testing CRISPR-based *LMNA* exon-removal and precise editing

Having generated L-CMD CRISPR-edited skeletal myogenic cells, we assessed whether some of the established phenotypic readouts (e.g. Figure 2) would be ameliorated following gene editing. Examination of nuclear deformities in *LMNA* L302P, Δexon 5 and corrected (edited) e-WT cells revealed a significant amelioration of myonuclear shape phenotypes in e-WT, with proportion of "Normal" myonuclei in the e-WT line was similar to that of Control 1 and Control 2 cell lines (Figure 2B), indicating a reversion of myonuclear shape phenotypes (Figure 5B). Δexon 5 cells showed a trend towards amelioration of nuclear deformities, with the proportion of "Deformed" myonuclei in L302P (30.24 ± 5.17 %) and Δexon 5 (22.72 ± 3.81 %) cell lines higher than was observed in e-WT myonuclei (11.53 ± 1.79 %). Similarly, "Blebbed" myonuclei were present at higher proportions in L302P (4.33 ± 2.66 %) and

Δexon 5 (2.79 ± 1.25 %) than in e-WT (0.58 ± 0.26 %) cells. “Elongated” myonuclei were present in L302P (4.44 ± 4.62 %) and Δexon 5 (1.63 ± 1.01 %) cells but were completely absent from e-WT cells. Similarly, in keeping with our results in Figure 2B, L302P had a low proportion of “String” myonuclei (0.51 ± 0.5 %), as did Δexon 5 (0.43 ± 0.74 %), while these myonuclei were absent in e-WT cells (Figure 5B).

For an objective readout, the NCR was quantified comparing Δexon 5 and e-WT nuclei to *LMNA* L302P nuclei (Figure 5C). L302P myonuclei and non-myonuclei showed reduced circularity (myonuclei: 0.727 ± 0.063; non-myonuclei: 0.676 ± 0.057). Δexon 5 myonuclei did not achieve significant improvement of circularity scores (myonuclei: 0.760 ± 0.098; non-myonuclei: 0.692 ± 0.08). In contrast, precise correction of the L302P mutation in the e-WT line significantly ameliorated NCR in both myonuclei and non-myonuclei (myonuclei: 0.781 ±0.044; non-myonuclei: 0.781 ± 0.054). Analysis of myonuclear perimeter showed no significant difference between L302P and either Δexon 5 or e-WT, whereas perimeter of e-WT non-myonuclei (56.58 ± 0.78 μm) were significantly shorter versus L302P (63.21 ± 3.49 μm), while no significant amelioration was observed in Δexon 5 (60.31 ± 4.76 μm)(area did not differ significantly in any of the groups; Figure S4).

We then analysed lamin mislocalisation in CRISPR-edited cells (Figure 5D). Similar to nuclear shape analyses, there was no statistically significant amelioration of LAMIN A/C mislocalisations compared to L302P (23.2 ± 8.04 %) in Δexon 5 myonuclei (13.8 ± 5.75 %; Figure 5E). In contrast, e-WT myonuclei showed significant amelioration of LAMIN A/C mislocalisation (1.07 ± 0.576 %). Although not statistically significant (p=0.092), mean LAMIN B1 mislocalisation was increased in Δexon 5 myonuclei (25.4 ± 9.40 %) compared to L302P myonuclei (12.5 ± 3.43 %; Figure 5F). In contrast, e-WT myonuclei LAMIN B1 mislocalisations were almost completely

ameliorated (1.05 ± 0.50 %). Finally, we analysed the formation of nucleoplasmic reticula in the myonuclei of L302P and CRISPR-corrected cells (Figure 5G). Similar to other analyses, nucleoplasmic reticulum formation was not ameliorated in Δexon 5 myonuclei (17.86 ± 2.37 %) compared to L302P (17.35 ± 1.56 %). Myonuclei positive for nucleoplasmic reticulum were increased in e-WT (42.69 ± 5.68 %) myonuclei, indicating that these structures are stabilised in cells expressing wild type LAMIN A/C.

Having established that e-WT cells ameliorate characteristic myonuclear morphological and protein localisation, we next utilised the 3D engineered muscle platform to examine amelioration of myonuclear phenotypes in a physiologically relevant culture system (Figure S4C). Analysis of myonuclear shape in engineered muscles showed that both Δexon 5 (18.72 ± 0.16 %) and e-WT (18.79 ± 0.99 %) nuclei were significantly less elongated than L302P (22.86 ± 2.56 %), demonstrating amelioration of nuclear elongation phenotypes with CRISPR-based interventions in the 3D culture system (Figure 5H).

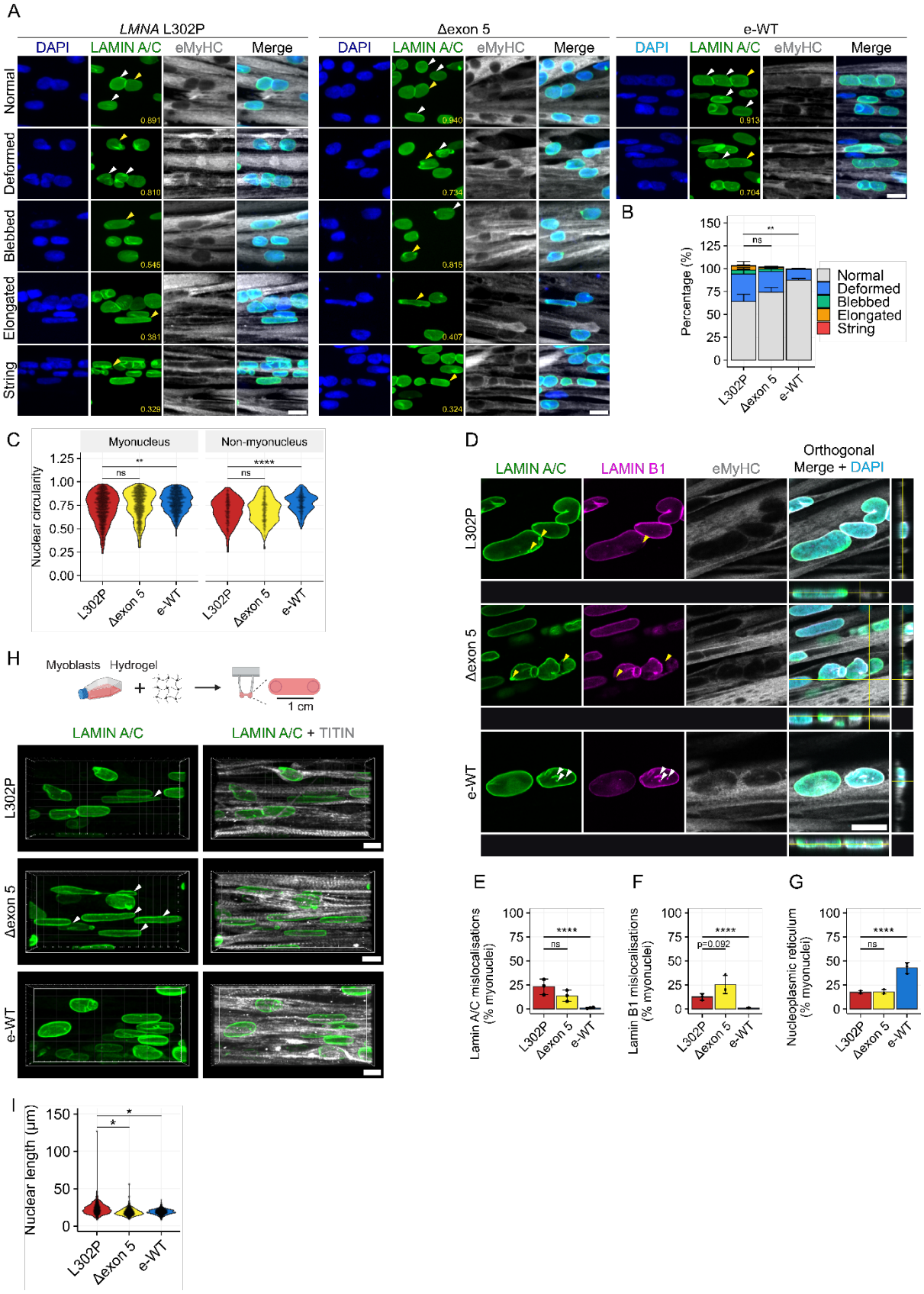
A
LMNA L302P
Δexon 5
e-WT
DAPI
LAMIN A/C
eMyHC
Merge
Normal
Deformed
Blebbed
Elongated
String
B
Percentage (%)
Normal
Deformed
Blebbed
Elongated
String
L302P
Δexon 5
e-WT
C
Myonucleus
Non-myonucleus
Nuclear circularity
D
LAMIN A/C
LAMIN B1
eMyHC
Orthogonal
Merge + DAPI
E
F
G
Lamin A/C mislocalisations (% myonuclei)
Lamin B1 mislocalisations (% myonuclei)
Nucleoplasmic reticulum (% myonuclei)
H
Myoblasts
Hydrogel
1 cm
LAMIN A/C
LAMIN A/C + TITIN
I
Nuclear length (µm)

Figure 5. Phenotypic amelioration of CRISPR-edited *LMNA* L302P myonuclei.

(A) Immunostain of LAMIN A/C and embryonic myosin heavy chain (eMyHC) showing representative images of five nuclear morphology classifications are displayed: Normal, Deformed, Blebbed, Elongated, and String. Scale bar 20 µm.

(B) Proportion of nuclear shape classifications in myotube nuclei. Nuclei with more than one type of abnormality (e.g. elongated and deformed) were scored twice meaning totals can exceed 100%. Nuclei were considered elongated if they had a major axis length >30 µm. Number of normal shaped nuclei were compared between LMNA-mutants and controls for statistics. Fractional logistic regression with Tukey's correction for pairwise comparisons. Three independent passages were analysed per cell line (N=3). 189 - 365 myotube nuclei were analysed per cell line, per repeat. ns $p>0.05$; ** $p<0.01$. Data presented as stacked bar chart. Whiskers show standard deviation.

(C) Graphs showing quantification of nuclear circularity. Beta regression with Bonferroni correction for pairwise comparisons. Data presented as scatter plots showing measurements of all nuclei across repeats with violin plots showing distribution of measurements. Three independent passages were analysed per cell line (N=3). 181 - 301 myotube nuclei and 32 - 108 non-myotube nuclei were analysed per cell line, per repeat. ns $p\geq0.05$; * $p<0.05$; ** $p<0.01$; *** $p<0.001$; **** $p<0.0001$.

(D) Representative immunostain of LAMIN A/C, LAMIN B1 and eMyHC. Counterstained with DAPI. Z-stack images of control and LMNA-mutant nuclei are displayed as a single Z-slice, with orthogonal view. White arrowheads indicate nucleoplasmic reticulum, yellow arrows indicate LAMIN mislocalisations. Scale bar 20 µm.

(E, F) LAMIN A/C (E) and LAMIN B1 (F) mislocalisation. Fractional logistic regression with Tukey's post hoc test for pairwise comparisons. Three independent passages were analysed per cell line (N = 3). A total of 237 - 340 nuclei were analysed per cell line, per repeat. **** $p < 0.0001$. Dots represent the mean value of one replicate. Whiskers indicate the standard deviation.

(G) Quantification of nucleoplasmic reticulum positive nuclei in control and LMNA-mutant myotube nuclei. Fractional logistic regression with Tukey's post hoc test for pairwise comparisons. Three independent passages were analysed per cell line (N = 3). 237 - 340 nuclei were analysed per cell line, per repeat. * $p<0.05$; ** $p<0.01$; *** $p<0.001$. Dots show mean value of one replicate. Whiskers show standard deviation.

(H) Schematic diagram showing generation of 3D engineered muscles. Immunostain for LAMIN A/C and TITIN in 3D engineered muscles. Scale bar 5 µm.

(I) Graphs showing quantification of myonuclear length. One-way ANOVA with Tukey's correction for pairwise comparisons. Data presented as scatter plots showing measurements of all nuclei across repeats with violin plots showing distribution of measurements. Three independent passages were analysed per cell line (N=3). 88 - 357 were analysed per cell line, per repeat. * $p<0.05$.

DISCUSSION

Models of skeletal muscle laminopathies have relied primarily on platforms which do not recapitulate human genetics (mouse, *Drosophila* etc.), are not in the context of the primarily affected tissue (fibroblasts, cell lines e.g. HEK / HeLa) or are difficult to

access (e.g. biopsies). Immortalised myoblasts address some of those limitations, but do not allow studies into early pathogenic events (i.e. during developmental myogenic specification). Use of iPSC-based models can address most of these challenges and in this study, we focused on harnessing their potential to gain further insights into the pathogenesis of laminopathies, as well as to model response to genetic therapies.

Previous studies showed impaired myogenic differentiation in *Lmna*-mutant myoblasts[22,31,32]. Overexpression of *LMNA* mutations W520S or R453W in C2C12 cells,[33,37] K32del mouse primary myoblasts and K32del, R249W and L380S human immortalised myoblasts all displayed impaired myogenic differentiation[5,27,38]. Transcriptional and epigenetic mechanisms leading to expression of non-muscle genes have been suggested as causative mechanisms[19]. However, most studies focus on murine myogenesis and those based upon human cells likely model adult/regenerative myogenesis. iPSCs from several congenital laminopathy phenotypes, allowed us to examine whether perturbations of myogenesis occurred at earlier developmental stages. Exogenous myogenic factors were not used in hiPSCs to avoid confounding factors that may compensate any myogenic defect. Using directed differentiation of hiPSCs as a synthetic model of human developmental myogenesis, we did not find overt defects in primary or secondary myogenesis. Thus, defects in myogenic differentiation and loss of muscle-specific gene expression could be more prevalent postnatally or require prolonged exposure cell to an abnormal nuclear lamina and its consequences, including abnormal chromatin configuration, DNA damage accumulation or nuclear ruptures.

Nuclear shape abnormalities are an established phenotype in striated muscle laminopathies reported *in vivo* and *in vitro*[4–10,39–41]. The K32del and R249W variants used here display nuclear shape abnormalities[4,5,42–44], and are associated with

significant clinical severity[45]. Abnormal nuclear morphometric parameters were also present in a novel line harbouring the *LMNA* L302P variant. Thus, our model recapitulated nuclear morphological abnormalities in all *LMNA*-mutant lines assessed, including nuclear elongation in 3D culture, demonstrating that it is a robust platform for modelling disease-associated pathological features.

Lamin mislocalisation contributes to weakening of the nuclear envelope and is associated with nuclear rupture. Additionally, lamin mislocalisation and aggregation are predictive of affected tissue type with most myopathic *LMNA* mutations showing aggregation[36]. Moreover, it has been suggested that mutant lamin A/C proteins causing aggregation lead to more severe L-CMD phenotypes[44]. Those findings were reproduced in our platform and, interestingly, iPSC-based disease modelling using developmentally relevant approaches for myogenic differentiation resulted in better capture of lamin protein mislocalisation than transgene-based approaches. For example, LAMIN A/C and B1 mislocalisation with *LMNA* K32del and R249W was not evident using a transgene-based iPSC differentiation protocol[9,46].

There was reduced formation of nucleoplasmic reticulum in *LMNA*-mutant myonuclei. These nuclear invaginations have reported roles in maintenance of nuclear architecture, nucleocytoplasmic transport, calcium signalling and DNA damage repair[47,48]. Accumulation of progerin at the nuclear envelope in Hutchinson-Gilford progeria syndrome (HGPS) increases the prevalence of nucleoplasmic reticulum in HGPS nuclei[49]. Furthermore, the EDMD-causing R453W and the FPLD2-causing R482W mutations also lead to an increase in nucleoplasmic reticulum in fibroblasts. In contrast, our observation that nucleoplasmic reticulum is reduced in *LMNA*-mutant myogenic cell nuclei suggests that these intranuclear structures might be destabilised by L-CMD-causing mutations.

An outstanding question is how changes in nuclear architecture affect transcriptional output. We found that dysmorphic nuclei remain transcriptionally active even in cases of severe deformity. This highlights the need for closer examination of chromatin organisation and transcriptional output in structurally compromised myonuclei. Our assessment of bulk transcriptional output to ascertain global changes in transcription in *LMNA*-mutant myogenic cells identified multiple hallmark gene sets related to inflammatory signalling were enriched in *LMNA*-mutant iPSC skeletal myogenic derivatives. This is consistent with observations in mouse *Lmna*-null and *Lmna*^{D300N} cardiac tissues[50,51], and muscle biopsies of L-CMD patients, where an atypically florid inflammatory infiltrate and fibrosis is often noted[52]. Moreover, this is also in keeping with high levels of proinflammatory and profibrotic cytokines reported in the serum of patients with muscle laminopathies, pointing to a cell autonomous source (i.e. muscle fibres) for some of those signals[53,54]. Interestingly, case-reports of beneficial corticosteroid therapy in some children with L-CMD support further investigations into this strategy as a possible therapeutic option targeting the inflammatory component of the disease[55].

A robust *in vitro* disease model should have sufficient resolution to predict outcomes of possible therapeutic interventions. We previously reported a potential exon-skipping strategy for pathogenic variants in *LMNA* exon 5, conducted primarily in mouse embryonic fibroblasts (MEFs)[8]; however, phenotypes differ between mouse and human[25]. Therefore, we used our model to examine exon-skipping and precise correction/editing as gene therapy strategies for L-CMD. Excision of *LMNA* exon 5 lead to LAMIN A/C production, nuclear envelope assembly and myogenic differentiation, inducing a trend towards amelioration in some myonuclear defects. Precise CRISPR-correction of the *LMNA*^{L302P} mutation completely reverted

myonuclear phenotypes to a state comparable with healthy controls, supporting further pre-clinical work to assess delivery modalities and gene editors capable of targeting and correcting pathogenic *LMNA* variants also in post-mitotic nuclei.

iPSC reprogramming of *LMNA*-mutant cells has been shown to reverse HGPS phenotypes, which are then reacquired upon differentiation[56]. This is likely due to LAMIN A/C expression being low to absent in pluripotent cells and upregulated upon differentiation. Here, we applied gene therapy approaches directly to iPSCs which we then differentiated into myogenic cells. Future work should examine the impact of similar gene therapies on cells which have a pre-established nuclear lamina, such as post-mitotic muscle tissue. LAMIN A/C proteins exhibit a long half-life[57] and so when gene therapy is applied to non-dividing cells, it may take some time for the newly repaired LAMIN A/C proteins to have an ameliorating effect on disease phenotypes[57].

Overall, here we provided evidence that hiPSCs and their myogenic derivatives can contribute to several key aspects of translational research in laminopathies, including: 1) diagnostics, such as detection of nuclear abnormalities in novel gene variants; 2) pathophysiology, including assessment of myogenic defects and proinflammatory signature; and 3) therapy development, via testing CRISPR-based gene editors. Together, this advances complex disease modelling in rare diseases.

MATERIALS AND METHODS

Cell lines and cultures

Two healthy control human iPSC lines were used: NCRM1 (https://hpscreg.eu/cell-line/CRMi003-A) and NCRM5 (https://hpscreg.eu/cell-line/CRMi001-A), referred to as Control 1 and 2 respectively. *LMNA* K32del (https://hpscreg.eu/cell-line/CMDi003-A)

and R249W (https://hpscreg.eu/cell-line/CMDi004-A) cell lines were kindly provided by Cellular Dynamics International Inc. (https://www.fujifilmcdi.com/) and Cure Congenital Muscular Dystrophy (CureCMD: https://www.curecmd.org/). iPSCs were generated by CDI by reprogramming samples provided by CureCMD (holder of clinical information) using episomal vectors. *LMNA* L302P iPSCs were generated by lentiviral expression of pluripotency genes (https://hpscreg.eu/cell-line/UCLi006-A; see below for details).

iPSCs were cultured in mTeSR Plus medium (STEMCELL Technologies, 100-0276), supplemented with 100 IU penicillin/streptomycin. Cells were grown on tissue culture plates coated in Matrigel (Corning, 354230/354231), diluted 1:100 in DMEM high glucose at 5% O_2 and 5% CO_2. Skeletal myogenic differentiation was performed using Myocea skeletal muscle differentiation kit (Myocea Inc., SKM01, SKM02) [34]. Briefly, iPSCs were dissociated in TrypLE Express (GIBCO, 12604-013) and 5,000 cells/cm^2 were seeded into matrigel coated plates. Cells were maintained in induction medium (SKM01) for 10 days, with medium changes every other day. At day 10, cells were passaged and plated on Matrigel coated plates at 5000 cells/cm^2 in Myoblast medium (SKM02). Cells were maintained for 8 days, with medium changes every other day. At day 8, cells were passaged and from this point, were maintained and passaged in tissue culture flasks without Matrigel in Myoblast medium. To differentiate myoblasts into multinucleated myotubes, myoblasts were passaged and plated on Matrigel coated plates at ~60,000 cells/cm^2 at a confluence of 95-100% after attachment. The next day, cells were switched to differentiation medium (DMEM high glucose (SIGMA, D5671-500mL), 2% horse serum (Euroclone), 1% Glutamax (Thermo Fisher Scientific, A5256701), 1% penicillin/streptomycin (GIBCO, 15070-063). In monlayer cultures,

cells were differentiated for 3-4 days. In 3D engineered muscles, cells were differentiated for 5-7 days with 3 parts differentiation medium, 1 part Myoblast medium.

HEK and HeLa cells were cultured in DMEM High glucose (Sigma, D5671-500mL), supplemented with 10% FBS (Life Technologies, A5670701), 2 mM Glutamax (Sigma, 35050061), 100 IU + 0.1 mg/mL penicillin/streptomycin (Sigma, P4333-100ML). Cells were grown at 37°C under ambient O_2 and 5% CO_2. Human cell work was conducted under the approval of the NHS Health Research Authority Research Ethics Committee reference no. 13/LO/1826; IRAS project ID no. 141100.

Generation and characterisation of *LMNA*^{L302P} hiPSCs

Reprogramming to pluripotency

LMNA^{L302P} dermal fibroblasts were kindly provided by Jean-Marie Cuisset (Centre de Référence des maladies neuromusculaires Nord/Est/Ile de France) under informed consent and reprogrammed using lentiviral vectors encoding MYC, SOX2, OCT3/4, and KLF4 under the control of CMV promoters (Kerafast) and Human iPSC Boost Supplement II kit (Merck Millipore, SCM094). Reprogramming was conducted on mitotically inactivated mouse embryonic feeder (MEF) based culture conditions with Knockout serum replacement medium (Knockout DMEM (Gibco, 10829018), 25% (v/v) KSR (Gibco, 10828028), 1% non-essential amino acids (Sigma, M7145-100ML), 2 mM Glutamax (Sigma, 35050061), 0.1 mM β-mercaptoethanol (Gibco, 21985023), 100 IU + 0.1 mg/mL penicillin/streptomycin (Sigma, P4333-100ML), 10 ng/mL bFGF (Gibco, 13256-029)) according to manufacturer's recommendations. 80,000 cells were plated in 6 well culture plates. Cells were transduced with the four viruses at MOI 30 in 1 mL of 10% DMEM (Dulbecco's modified eagle medium) with 8 µg/mL Polybrene

(hexadimethrine bromide, Sigma). For the viral transductions, heat inactivated DMEM 10% was used (FBS heat inactivated at 56 °C for 30 minutes, to inactivate complement factors). Cells were incubated with the viral mix for 8 hours, after which the medium was aspirated, cells washed three times with PBS, and fresh DMEM 10% added. On day 5 transduced cells were replated onto Matrigel coated plates on top of a layer of inactivated MEFs, with knockout serum replacement medium supplemented with Human iPSC Boost Supplement II kit. Two six well plates of MEFs were used to plate infected fibroblasts. Medium was changed every other day until day 25. Fresh MEFs were added to the wells on day 11. Small molecule supplementation was added to the media every other day until day 18. On day 25 the first iPSC colonies were isolated and picked manually to isolate from fibroblasts that had not been reprogrammed. Isolated colonies were plated onto freshly prepared plates of MEFs. Each picked colonies was cultured separately, to ensure clonal expansion. Three distinct clonal lines were expanded in knockout serum replacement medium on MEFs for ~4 passages, after which they were moved to feeder-free conditions with TESR-E8 medium and expanded on Matrigel following standard manufacturer's recommendations (Stem Cell Technologies).

Karyotype analysis

Karyotype analysis was performed by The Doctors Laboratory (TDL, London, UK). For *LMNA* L302P iPSCs, 7 cells were analysed. 5 showed a normal karyotype, with 2 having chromosome losses associated with preparation artefacts.

Alkaline phosphatase staining

Cells were washed with PBS, fixed with 4% PFA for 5 minutes and washed again with PBS. Cells were incubated for 20 minutes in alkaline phosphatase staining solution

(0.1 M Trizma hydrochloride, 0.1 M NaCl, 0.5 M $MgCl_2$, 0.5 % v/v µL Tween 20, 2 % v/v NBT/BCIP solution (18.75 mg/mL NBT, 9.4 mg/mL BCIP). Following incubation, cells were imaged with a dissecting microscope.

Embryoid body formation

iPSCs were detached with Gentle Cell Dissociation Reagent for 6 minutes at room temperature, after which it was aspirated, and TESR-E8 containing 4 mg/mL of Polyvinal alcohol and 3 µg/mL of ROCK inhibitor Y27362 (Calbiochem) was added. Cells were collected by scraping and transferred to a non-tissue culture treated plate, to allow EBs to form in suspension. The following day the medium was changed to TESR-E6 (Stem Cell Technology), for 5 days, with media changes every other day. After five days the medium was switched to spontaneous differentiation medium (DMEM 20 %), although cells were not transferred to adherent plates (tissue culture treated), the EBs adhered to the non-tissue culture treated plate after the medium was switched to DMEM 20%. After 7 days, the medium was aspirated, replaced with PBS and cells collected by scraping, cells were spun at 232 g, transferred to a 1 mL Eppendorf vial and spun again at 10,000 g. RNA was then extracted from the pellet, as detailed in section 2.8.

3D engineered skeletal muscle constructs

3D engineered muscles were constructed as previously described[30,58]. Briefly, myoblasts were pre-treated with 10 µm ROCK inhibitor for 2 hours prior to passaging. Cells were counted (1 million/construct) and centrifuged before being placed on ice. 100 µL of heat-inactivated Myoblast medium was added, after which, 10% Matrigel and 3.5 mg/mL human fibrinogen (Baxter) were added. Inactivated medium was added

to the calculated final volume and for each muscle, 113uL was individually added to aliquoted thrombin (Baxter). The final mixture for each muscle was decanted into 2% UltraPure agarose in DPBS (Invitrogen, 16500-500) moulds containing silicon posts (EHT Technologies, GmbH Hamburg). Constructs were placed at 37°C, 5% CO2 for 2 hours before DMEM high glucose was added onto each muscle. After a further 10-minute incubation at 37°C, posts were removed from the moulds and muscles were visually inspected for successful polymerisation. Muscles were placed into a fresh 24 well plate containing pre-warmed Myoblast medium supplemented with 33 µg/µL aprotinin (Sigma Aldrich, A3428-10MG). Muscle constructs were cultured for 2 days in Myoblast medium at 37°C, 5% CO_2 after which the medium was switched to differentiation medium.

Generation of CRISPR-corrected *LMNA*^{L302P} iPSCs (e-WT)

CRISPR correction of *LMNA* L302P iPSCs was performed by Synthego. *LMNA* L302P iPSCs were sent as frozen stocks and homology directed repair was performed. sgRNA and donor template used are indicated in Supplementary table 1.

CRISPR sgRNA and pegRNA design

sgRNAs were designed using Benchling CRISPR design tool using cutting efficiency calculations based on Doencsh *et al*.[59] sgRNAs were ordered from Synthego with 2'-O-Methyl analogues and 3' phosphorothioate bond modifications. sgRNAs used are indicated in Supplementary table 2.

Nucleofection

Nucleofection of iPSCs was performed using an Amaxa 4D nucleofector X unit (Lonza, AAF-1003X) and the P3 Primary Cell Kit (Lonza, V4XP-3032). Synthego sgRNAs were

hydrated to 100 μM in TE buffer. 2 hours prior to nucleofection, iPSCs were treated with a final concentration of 10 μM ROCK inhibitor (Cell Guidance Systems, SM02-5). 1 hour prior to nucleofection, 6 well plates were coated with Matrigel. For excision of *LMNA* exon 5 sequence, 1.5 μL of each sgRNA was premixed with 2 μL 20 μM SpyCas9 (NEB, M0646T) to a final concentration of 300 pmol gRNA (150 pmol each) and 40 pmol SpyCas9 respectively. The mixture was incubated at room temperature for 10 minutes and was transferred to ice. Cells were detached with TrypLE Express for 5 minutes and neutralised with premade mTesr1 + CloneR2 (STEMCELL Technologies, 100-0691). 250,000 cells were counted per reaction and transferred to separate 1.5 mL Eppendorf tubes. Cells were resuspended in 20 μL P3 primary solution and mixed with pre-made RNP complex. The mixture was transferred to nucleofector cuvettes and nucleofected using program CA137. Pre-warmed mTesr1 + CloneR2 was added to the cuvette and incubated for 5 minutes before cells were transferred drop-wise to 6 well cell culture dishes with pre-warmed mTesr1 + CloneR2. Cells were maintained for 3 days before being dissociated using TrypLE Express. Half of the cells were taken for cryopreservation, and the other half was used for DNA extraction and PCR. Once genome editing had been confirmed by PCR, cells were thawed and expanded using standard iPSC culture techniques.

Single cell cloning

Single cell sorting of iPSCs was carried out in the Flow Cytometry facility at the Francis Crick Institute on a FACS ARIA II. Prior to dissociation, cells were treated for 2 hours with 10 μM ROCK inhibitor. Cells were dissociated with TrypLE Express for 3-5 minutes at 37°C, centrifuged and resuspended in 1 mL of mTesr1 + CloneR2 (STEMCELL Technologies, 100-0691). Cells were passed through a FACS tube filter and were transported for sorting. Cell were cloned into 96 well plates pre-coated with

Matrigel and filled with mTesr1 + CloneR2 using a 100µm nozzle. Cells were subsequently fed every two days with mTesr1 + CloneR2 thereafter. Cells were monitored regularly and approximately 1 to 2 weeks later, surviving colonies were expanded to a 24 well and then 12 well plate format in this medium using standard iPSC culture techniques. Once ready to passage in a 12 well plate, half the cells were cryopreserved and half were taken for DNA isolation and PCR-based screening.

DNA / RNA extraction and cDNA preparation

DNA was extracted from cells using DNAeasy blood and tissue kit (QIAGEN, 69506) as described in the protocol. DNA was eluted in elution buffer (EB). DNA concentration and purity was verified by nanodrop. RNA extraction was performed using RNAeasy Micro Kit (QIAGEN, 74004) as described in the protocol, with the exception that all centrifugation times were doubled. RNA was eluted in RNase-free water and quantified by Nanodrop. cDNA was prepared from extracted DNA using High-Capacity RNA-to-cDNA Kit (Applied Biosystems, 4387406) as described in the protocol.

Sanger sequencing

PCR for Sanger sequencing was carried out using Promega GoTaq G2 Hot Start Taq Polymerase (Promega, M7422) according to the manufacturer's protocol. Samples were purified using GeneJet PCR Purification Kit (Thermo Fisher Scientific, K0701). Sanger sequencing was performed by GENEWIZ LLC. Primer sequences are provided in Supplementary Table 3.

RNA-sequencing

RNA was extracted for RNA sequencing using RNAeasy Micro Kit (QIAGEN, 74004). Extracted RNA was quantified using a Bioanalyzer. RNAseq libraries were prepared using NEBNext Ultra II Directional PolyA mRNA kit within the Genomics facility at The Francis Crick Institute. Sequencing was performed in paired-end 100bp on Novaseq S2 platform in the Genomics facility in The Francis Crick Institute to a depth of 25 million reads per sample. RNA sequencing data was processed using nf-core/rnaseq pipeline version 3.13.2[60]. The pipeline was executed with Nextflow version 23.10.0 on The Francis Crick Institute NEMO high performance computing cluster. Reads were aligned to the GRCh38 genome using Star. Gene expression quantification was performed using Salmon and quality control of raw and processed reads was performed with MultiQC. Differential gene expression analysis was performed using DESeq2 in RStudio running R v4.3.1.

AlphaFold protein structural prediction

For protein modelling, AlphaFold 2 v2.3.1 was run on The Francis Crick Institute NEMO high performance computing cluster. The predicted aligned error (PAE) and predicted local distance difference test were analysed using UCSF ChimeraX and PyMOL to validate the model.

Protein extraction and western blot

Cells were cultured and differentiated as described previously in a 6 well culture plate. Media was aspirated and the plate was placed directly in the -80°C freezer. For protein extraction, 500 µL Laemelli buffer solution (50 mM Tris-HCl pH 6.8, 20% glycerol, 2% SDS was added directly onto the culture dish and cells were scraped and transferred

to an Eppendorf tube. Cells were than boiled at 95°C for 5 minute and placed on ice for 2-3 minutes. Samples were then centrifuged briefly. Protein quantification was carried out using BIORAD Protein Assay Kit (BIORAD, 5000002) as per the manufacturer's protocol. Protein concentration was determined using BSA standards diluted in Laemelli buffer. Western blot was carried out using 40µg of protein for each sample. Samples were diluted with pre-made 4x loading buffer (BIORAD, 1610747), supplemented with DTT to a final concentration of 1 mM and boiled for 5 minutes at 95°C before briefly centrifuging and placing on ice. Samples were run on 4-20% Mini-PROTEAN TGX Precast protein gels (BIORAD, 4561094). Gels were run at 100 V for 10 minutes and 120 V thereafter for 2 hours in protein running buffer with 1% SDS. Samples were transferred to nitrocellulose membranes using iBlot2 system (Invitrogen, IB24001) for 6 minutes at 25 V according to manufacturer's protocol. Membranes were blocked for 1 hour in 5% w/v milk diluted in Tris-buffered saline with tween 20 (TBST; 20mM Tris ph7.5, 150mM NaCl, 1% (v/v) tween 20). LAMIN A/C primary antibody (SLS, SAB4200236-200UL) was used at a concentration of 1:500 in milk overnight at 4°C on a gentle rocker. The next day, membranes were washed 3 times for 5 minutes with TBST. Secondary antibody (Goat Anti-Mouse IgG (H + L)-HRP Conjugate (BIORAD, #1706516)) was diluted in 5% milk diluted in TBST for 1 hour at 4°C on a gentle rocker. Membranes were washed with TBST 3 times for 5 minutes with TBST. Bands were visualised using Amersham ECL western Blotting Detection Reagents (GE Healthcare, 28980926) according to the manufacturer's instructions and imaged using BIORAD Chemidoc MP Imaging System.

Immunostaining

Cells were fixed with 4% paraformaldehyde (PFA; Boster, AR1068) for 10 minutes at room temperature and washed with PBS. Cells were permeabilized in PBS with 0.2% Trition-X-100 (Sigma Aldrich, T8787-50mL) and 1% bovine serum albumin (BSA; Sigma Aldrich, A3294-50G) for 40 minutes at room temperature. Cells were blocked for 40 minutes at room temperature with permeabilization buffer supplemented with 10% goat serum (Sigma Aldrich, G9023-10mL). Primary antibodies were diluted in permeabilization buffer and incubated overnight at 4°C. The next day, primary antibodies were removed and cells washed 3 times for 5 minutes in PBS with 0.2% Triton-X-100. Secondary antibodies were diluted in the same solution and incubated for 1 hour at room temperature while blocked from light. Afterwards, cells were washed three times with PBS and stored at 4°C until imaged.

3D engineered muscles were immunolabelled as previously described[57]. Briefly, muscles were fixed in 4% PFA while still attached to posts for 3 hours at 4°C. Muscles were washed with PBS before being removed from posts and placed into blocking buffer (0.05 M TBS (1x) pH7.4, 10% FBS, 1% BSA, 0.5% Triton-X-100) for 6 hours. Incubation with primary antibodies was carried out in antibody buffer (blocking buffer without 10% FBS) overnight on a shaker at 4°C. The next day, 6 washes were applied throughout the day with 1x TBS. Secondary antibodies were diluted in antibody buffer overnight on a shaker at 4°C. The next day, muscles were washed 6 times with 1x TBS before the muscles were mounted onto cavity slides (MERCK Life Science Ltd. UK, BR475505-50EA) with mounting medium (SIGMA Aldrich, F4680-25mL).

Primary antibodies used in this study were: rabbit anti NANOG, 1:100 (Abcam ab800892); mouse IgG2B anti OCT3/4, 1:100 (Santa Cruz Biotechnology sc5297); rabbit anti SOX2, 1:200 (Abcam ab92494); mouse IgG2B anti LAMIN A/C, 1:250 (Invitrogen MA3100); rabbit anti LAMIN B1, 1:100 (Abcam ab16048); mouse IgG1 anti

MYH3, 1:9 (DSHB F1.652); rabbit anti NUP153, 1:100 (Abcam ab84872); mouse IgM anti TITIN, 1:100 (DSHB 9D10). Secondary antibodies used were all AlexaFluor (Life Technologies 1:500). When immunostain 3D engineered muscles, all antibody dilutions were halved.

Nascent RNA labelling

Nascent RNA was labelled using Click-iT™ RNA AlexaFluor 594 Imaging Kit (Thermo Fisher Scientific, C10330). Briefly, cells were differentiated into myotubes as previously described on µ-Plate 24 Well ibiTreat (Ibidi, 82426). Cells were incubated with 1 mM EU for 1 hour prior to fixation for 15 minutes in 4% PFA. Cells were washed with PBS and permeabilised with 0.5% Triton-X for 1 hour. Click-IT reaction cocktail was added to the cells for 30 minutes before washing with Click-IT reaction rinse buffer. Immunostain for LAMIN A/C and embryonic myosin heavy chain was then carried out as described previously.

Microscopy

For standard fluorescence microscopy, a Nikon Ti2 inverted microscope was used with Teledyne Photometrics Prime BSI scientific CMOS camera and ASI motorised XY stage with Piezo Z, controlled with Micro-Manager v2.0 software. Imaging was carried out using either Plan Fluor 10x 0.30NA Ph1 or Nikon CFI S Plan Fluor ELWD 20XC lens with 1.5x zoom for final magnification of 30x for nuclear shape measurements. Spinning disc imaging for analysis of LAMIN A/C and LAMIN B1 mislocalisations and nucleoplasmic reticulum were conducted on a Nikon Ti2 with Yokogawa CSU-W1 SORA scanhead, driven with NIS-Elements using 40x lens and

no additional zoom. The same microscope was used for imaging of 3D engineered muscles for the purpose of nuclear length measurements. For imaging of iPSC pluripotency markers in *LMNA* L302P iPSCs, a Leica DM16000B inverted microscope was used.

Analysis of nuclear morphology and LAMIN A/C localisation

Nuclear abnormalities were quantified by circling individual nuclei using the polygon tool in Fiji imaging software. For each nucleus the circularity (4π area/circumference2), major length, perimeter and area of the selected region was measured as described previously[61]. Nuclear abnormality classification was carried out in a blinded manner to prevent bias. Classes were calculated using the cell counter tool in Fiji imaging software. Classes are as follows: “Normal”, “Deformed”, “Blebbed”, “Elongated” or “String”. “Elongated” nuclei were classified as any nucleus above 30 μm which was validated empirically as being longer than myonuclei observed in control lines. Nuclear length measurements were conducted using the line segment tool in Fiji.

Analysis of lamin mislocalisations was carried out in a blinded manner. LAMIN A/C mislocalisations were typically observed as either aggregations, patchy signal or absence of signal in particular areas (usually at the nuclear envelope). LAMIN B1 mislocalisations were typically characterized by absence of signal in particular areas such as in locations of LAMIN A/C aggregates. In control nuclei, LAMIN A/C and LAMIN B1 signal perfectly overlap each other and so any LAMIN A/C or LAMIN B1 signal that did not overlap with one another in LMNA-mutant myonuclei were classified as being mislocalised.

To assess presence of nucleoplasmic reticulum, spinning disc Z-stacks were visualized as 3D structures using Imaris imaging software. Nucleoplasmic reticulum was identified as co-stained LAMIN A/C and LAMIN B1 signal traversing the nuclear interior. Nuclear folds, characterised by a long stretch of intranuclear LAMIN signal, were not classified as nucleoplasmic reticulum. The same image was also opened in Fiji imaging software and after visual examination in Imaris, myonuclei with and without nucleoplasmic reticulum were counted and quantified blindly.

Myonuclear length in 3D artificial muscle constructs were analysed using the line segment tool in Fiji imaging software. Lines were drawn from pole to pole of the nuclei along their major axis.

Statistical analyses

Statistics were performed in R (v.4.3.1) and GraphPad PRISM. Statistical comparisons and post-hoc tests used for pairwise comparisons are indicated within figure legends. For all statistical comparisons, a minimum of three biological replicates were performed.

ACKNOWLEDGEMENTS

We are grateful to Dr Jean-Marie Cuisset (Centre de Référence des maladies neuromusculaires Nord/Est/Ile de France), CureCMD, Cellular Dynamics and L-CMD patients and their families for providing cells. We thank members of the Tedesco lab for helpful feedback and discussion, Francesca Torri, Noreen Khokhar, Sara Maffioletti, Matt Renshaw (Crick CALM STP), James Campbell (Crick Bioinformatics STP) and the Crick Flow Cytometry and Advanced Sequencing STPs for experimental

support and Dr. Rabah Ben Yaou (Cente de Reserche en Myologie) for maintenance of the *LMNA* UMD database. This work was funded by: • Muscular Dystrophy UK (19GRO-PS48-0188-1); • The European Union (Horizon Europe project no. 101080690 – MAGIC). Views and opinions expressed are however those of the authors only and do not necessarily reflect those of the European Union or HADEA. Neither the European Union nor HADEA can be held responsible for them. This work is funded by the UK Research and Innovation (UKRI) under the UK government's Horizon Europe funding guarantee grant numbers 10078461, 10080927 and 10079726; • LifeArc (CMCK-UK.FID119430465); • the European Research Council (759108 – HISTOID); • Biotechnology and Biological Sciences Research Council (BB/J014567/1; BB/M009513/1) • AFM-Telethon (29063). FST also acknowledge support by The Francis Crick Institute, which receives its funding from Cancer Research UK , the UK Medical Research Council and the Wellcome Trust, and the National Institute for Health and Care Research (NIHR; the views expressed are those of the authors and not necessarily those of the National Health Service, the NIHR, or the Department of Health). For the purpose of Open Access, the author has applied a CC BY public copyright licence to any Author Accepted Manuscript version arising from this submission.

REFERENCES

1. Worman, H. J. Nuclear lamins and laminopathies. *Journal of Pathology* (2012) doi:10.1002/path.2999.
2. Quijano-Roy, S. *et al.* De novo LMNA mutations cause a new form of congenital muscular dystrophy. *Annals of Neurology* (2008) doi:10.1002/ana.21417.

3. Ben Yaou, R. *et al.* International retrospective natural history study of LMNA-related congenital muscular dystrophy. *Brain Commun* **3**, fcab075 (2021).
4. Bertrand, A. T. *et al.* Cellular microenvironments reveal defective mechanosensing responses and elevated YAP signaling in LMNA-mutated muscle precursors. *Journal of Cell Science* **127**, 2873–2884 (2014).
5. Gómez-Domínguez, D. *et al.* Consequences of Lmna Exon 4 Mutations in Myoblast Function. *Cells* (2020) doi:10.3390/cells9051286.
6. Lammerding, J. *et al.* Lamin A/C deficiency causes defective nuclear mechanics and mechanotransduction. *Journal of Clinical Investigation* (2004) doi:10.1172/JCI200419670.
7. Park, Y. E. *et al.* Nuclear changes in skeletal muscle extend to satellite cells in autosomal dominant Emery-Dreifuss muscular dystrophy/limb-girdle muscular dystrophy 1B. *Neuromuscular Disorders* (2009) doi:10.1016/j.nmd.2008.09.018.
8. Scharner, J., Figeac, N., Ellis, J. A. & Zammit, P. S. Ameliorating pathogenesis by removing an exon containing a missense mutation: a potential exon-skipping therapy for laminopathies. *Gene Ther* **22**, 503–515 (2015).
9. Steele-Stallard, H. B. *et al.* Modeling skeletal muscle laminopathies using human induced pluripotent stem cells carrying pathogenic LMNA mutations. *Frontiers in Physiology* (2018) doi:10.3389/fphys.2018.01332.
10. Walker, S. G., Langland, C. J., Viles, J., Hecker, L. A. & Wallrath, L. L. Drosophila Models Reveal Properties of Mutant Lamins That Give Rise to Distinct Diseases. *Cells* **12**, 1142 (2023).
11. Wang, Y., Herron, A. J. & Worman, H. J. Pathology and nuclear abnormalities in hearts of transgenic mice expressing M371K lamin A encoded by an LMNA mutation causing Emery–Dreifuss muscular dystrophy. *Human Molecular Genetics* **15**, 2479–2489 (2006).
12. Méjat, A. *et al.* Lamin A/C–mediated neuromuscular junction defects in Emery-Dreifuss muscular dystrophy. *Journal of Cell Biology* **184**, 31–44 (2009).

13. De vos, W. H. *et al.* Repetitive disruptions of the nuclear envelope invoke temporary loss of cellular compartmentalization in laminopathies. *Human Molecular Genetics* (2011) doi:10.1093/hmg/ddr344.
14. Cheedipudi, S. M. *et al.* Genomic Reorganization of Lamin-Associated Domains in Cardiac Myocytes Is Associated With Differential Gene Expression and DNA Methylation in Human Dilated Cardiomyopathy. *Circulation research* (2019) doi:10.1161/CIRCRESAHA.118.314177.
15. Cheedipudi, S. M., Asghar, S. & Marian, A. J. Genetic Ablation of the DNA Damage Response Pathway Attenuates Lamin-Associated Dilated Cardiomyopathy in Mice. *JACC: Basic to Translational Science* **7**, 1232–1245 (2022).
16. Shah, P. *et al.* Nuclear Deformation Causes DNA Damage by Increasing Replication Stress. *Current Biology* **31**, 753-765.e6 (2021).
17. Sebestyén, E. *et al.* SAMMY-seq reveals early alteration of heterochromatin and deregulation of bivalent genes in Hutchinson-Gilford Progeria Syndrome. *Nat Commun* **11**, 6274 (2020).
18. Ikegami, K., Secchia, S., Almakki, O., Lieb, J. D. & Moskowitz, I. P. Phosphorylated Lamin A/C in the Nuclear Interior Binds Active Enhancers Associated with Abnormal Transcription in Progeria. *Developmental Cell* (2020) doi:10.1016/j.devcel.2020.02.011.
19. Bianchi, A. *et al.* Dysfunctional polycomb transcriptional repression contributes to lamin A/C-dependent muscular dystrophy. *Journal of Clinical Investigation* (2020) doi:10.1172/JCI128161.
20. Salvarani, N. *et al.* The K219T-Lamin mutation induces conduction defects through epigenetic inhibition of SCN5A in human cardiac laminopathy. *Nature Communications* (2019) doi:10.1038/s41467-019-09929-w.
21. Shah, P. P. *et al.* Pathogenic LMNA variants disrupt cardiac lamina-chromatin interactions and de-repress alternative fate genes. *Cell Stem Cell* (2021) doi:10.1016/j.stem.2020.12.016.

22. Cesarini, E. *et al.* Lamin A/C sustains PcG protein architecture, maintaining transcriptional repression at target genes. *Journal of Cell Biology* (2015) doi:10.1083/jcb.201504035.
23. Chandran, S. *et al.* Suppression of myopathic lamin mutations by muscle-specific activation of AMPK and modulation of downstream signaling. *Human Molecular Genetics* (2019) doi:10.1093/hmg/ddy332.
24. de las Heras, J. I. *et al.* Metabolic, fibrotic and splicing pathways are all altered in Emery-Dreifuss muscular dystrophy spectrum patients to differing degrees. *Human Molecular Genetics* **32**, 1010–1031 (2023).
25. Zhang, H., Kieckhaefer, J. E. & Cao, K. Mouse models of laminopathies. *Aging Cell* (2013) doi:10.1111/acel.12021.
26. Schwartz, C. *et al.* Lamins and nesprin-1 mediate inside-out mechanical coupling in muscle cell precursors through FHOD1. *Sci Rep* **7**, 1253 (2017).
27. Owens, D. J. *et al.* Lamin-Related Congenital Muscular Dystrophy Alters Mechanical Signaling and Skeletal Muscle Growth. *Int J Mol Sci* **22**, 306 (2020).
28. Owens, D. J. *et al.* Lamin Mutations Cause Increased YAP Nuclear Entry in Muscle Stem Cells. *Cells* **9**, 816 (2020).
29. Rose, N. *et al.* Bioengineering a miniaturized in vitro 3D myotube contraction monitoring chip to model muscular dystrophies. *Biomaterials* **293**, 121935 (2023).
30. Maffioletti, S. M. *et al.* Three-Dimensional Human iPSC-Derived Artificial Skeletal Muscles Model Muscular Dystrophies and Enable Multilineage Tissue Engineering. *Cell Reports* **23**, 899–908 (2018).
31. Frock, R. L. *et al.* Lamin A/C and emerin are critical for skeletal muscle satellite cell differentiation. *Genes and Development* (2006) doi:10.1101/gad.1364906.
32. Cohen, T. V. *et al.* Defective skeletal muscle growth in lamin A/C-deficient mice is rescued by loss of lap2α. *Human Molecular Genetics* (2013) doi:10.1093/hmg/ddt135.
33. Favreau, C., Higuet, D., Courvalin, J.-C. & Buendia, B. Expression of a Mutant Lamin A That Causes Emery-Dreifuss Muscular Dystrophy Inhibits In Vitro Differentiation of

C2C12 Myoblasts. *Molecular and Cellular Biology* (2004) doi:10.1128/mcb.24.4.1481-1492.2004.

34. Caron, L. *et al.* A Human Pluripotent Stem Cell Model of Facioscapulohumeral Muscular Dystrophy-Affected Skeletal Muscles. *STEM CELLS Translational Medicine* (2016) doi:10.5966/sctm.2015-0224.
35. Tiwari, V., Alam, M. J., Bhatia, M., Navya, M. & Banerjee, S. K. The structure and function of lamin A/C: Special focus on cardiomyopathy and therapeutic interventions. *Life Sciences* **341**, 122489 (2024).
36. Anderson, C. L. *et al.* Most myopathic lamin variants aggregate: a functional genomics approach for assessing variants of uncertain significance. *npj Genom. Med.* **6**, 1–11 (2021).
37. Markiewicz, E., Ledran, M. & Hutchison, C. J. Remodelling of the nuclear lamina and nucleoskeleton is required for skeletal muscle differentiation in vitro. *Journal of Cell Science* **118**, 409–420 (2005).
38. Pilat, U. *et al.* Muscle dystrophy-causing ΔK32 lamin A/C mutant does not impair functions of nucleoplasmic LAP2α - lamin A/C complexes in mice. *Journal of Cell Science* jcs.115246 (2013) doi:10.1242/jcs.115246.
39. Earle, A. J. *et al.* Mutant lamins cause nuclear envelope rupture and DNA damage in skeletal muscle cells. *Nat. Mater.* **19**, 464–473 (2020).
40. Chen, N. Y. *et al.* Fibroblasts lacking nuclear lamins do not have nuclear blebs or protrusions but nevertheless have frequent nuclear membrane ruptures. *Proceedings of the National Academy of Sciences* **115**, 10100–10105 (2018).
41. Lammerding, J. *et al.* Lamins A and C but Not Lamin B1 Regulate Nuclear Mechanics*. *Journal of Biological Chemistry* **281**, 25768–25780 (2006).
42. Muchir, A. *et al.* Nuclear envelope alterations in fibroblasts from patients with muscular dystrophy, cardiomyopathy, and partial lipodystrophy carrying lamin A/C gene mutations. *Muscle and Nerve* (2004) doi:10.1002/mus.20122.

43. Scharner, J. *et al.* Novel LMNA mutations in patients with Emery-Dreifuss muscular dystrophy and functional characterization of four LMNA mutations. *Human Mutation* (2011) doi:10.1002/humu.21361.
44. Bertrand, A. T. *et al.* Lamin A/C Assembly Defects in LMNA-Congenital Muscular Dystrophy Is Responsible for the Increased Severity of the Disease Compared with Emery-Dreifuss Muscular Dystrophy. *Cells* (2020) doi:10.3390/cells9040844.
45. Ben Yaou, R. *et al.* International retrospective natural history study of LMNA-related congenital muscular dystrophy. *Brain Commun* **3**, fcab075 (2021).
46. Maffioletti, S. M. *et al.* Efficient derivation and inducible differentiation of expandable skeletal myogenic cells from human ES and patient-specific iPS cells. *Nature Protocols* (2015) doi:10.1038/nprot.2015.057.
47. Stiekema, M. *et al.* The Role of Lamins in the Nucleoplasmic Reticulum, a Pleiomorphic Organelle That Enhances Nucleo-Cytoplasmic Interplay. *Front Cell Dev Biol* **10**, 914286 (2022).
48. Shokrollahi, M. *et al.* DNA double-strand break–capturing nuclear envelope tubules drive DNA repair. *Nat Struct Mol Biol* **31**, 1319–1330 (2024).
49. McClintock, D., Gordon, L. B. & Djabali, K. Hutchinson–Gilford progeria mutant lamin A primarily targets human vascular cells as detected by an anti-Lamin A G608G antibody. *Proc Natl Acad Sci U S A* **103**, 2154–2159 (2006).
50. Coste Pradas, J. *et al.* Identification of Genes and Pathways Regulated by Lamin A in Heart. *Journal of the American Heart Association* **9**, e015690 (2020).
51. DNA Damage Response/TP53 Pathway Is Activated and Contributes to the Pathogenesis of Dilated Cardiomyopathy Associated With LMNA (Lamin A/C) Mutations. https://www.ahajournals.org/doi/epub/10.1161/CIRCRESAHA.118.314238 doi:10.1161/CIRCRESAHA.118.314238.
52. Komaki, H. *et al.* Inflammatory changes in infantile-onset LMNA-associated myopathy. *Neuromuscular Disorders* **21**, 563–568 (2011).

53. Cappelletti, C. *et al.* Cytokine Profile in Striated Muscle Laminopathies: New Promising Biomarkers for Disease Prediction. *Cells* **9**, 1532 (2020).
54. Bernasconi, P. *et al.* Elevated TGF β2 serum levels in Emery-Dreifuss Muscular Dystrophy: Implications for myocyte and tenocyte differentiation and fibrogenic processes. *Nucleus* **9**, 337–349 (2018).
55. Garcia, M. G. *et al.* P431 Steroid treatment may change natural history in congenital laminopathies. *Neuromuscular Disorders* **33**, S160 (2023).
56. Liu, G.-H. *et al.* Recapitulation of premature aging with iPSCs from Hutchinson-Gilford progeria syndrome. *Nature* **472**, 221–225 (2011).
57. Hasper, J. *et al.* Long lifetime and tissue-specific accumulation of lamin A/C in Hutchinson–Gilford progeria syndrome. *Journal of Cell Biology* **223**, e202307049 (2023).
58. Pinton, L. *et al.* 3D Human Induced Pluripotent Stem Cell-derived Bioengineered Skeletal Muscles for Tissue, Disease and Therapy Modelling. *Nature Protocols* (2023) doi:https://doi.org/10.21203/rs.3.pex-2034/v1.
59. Doench, J. G. *et al.* Optimized sgRNA design to maximize activity and minimize off-target effects of CRISPR-Cas9. *Nat Biotechnol* **34**, 184–191 (2016).
60. Ewels, P. A. *et al.* The nf-core framework for community-curated bioinformatics pipelines. *Nat Biotechnol* **38**, 276–278 (2020).
61. Goldman, R. D. *et al.* Accumulation of mutant lamin A causes progressive changes in nuclear architecture in Hutchinson–Gilford progeria syndrome. *Proceedings of the National Academy of Sciences* **101**, 8963–8968 (2004).